POLITECNICO DI TORINO

Master Degree in Mechatronic Engineering

Master Degree Thesis

Design and validation of a dynamic optical system for beam monitoring and automatic focus compensation

Supervisors
Prof. Guido Perrone
Ing. Sabina Zaimovic

Candidate
Alessandro Scaglia

July 2025

Abstract

Owing to the increase in laser-based metal additive manufacturing technologies, it becomes necessary to understand the main process parameters leading to flaw formation, so that proper strategies can be adopted in order to tackle them. Laser powder interaction at the melt pool level is one of the most critical aspects to deal with, since the characteristics of the molten region, such as its size and shape, directly impact micro- and macro-structural properties of the built part. Hence, achieving precise focus control, in presence of mechanical and thermal effects causing unintended shifts during operation, is essential to ensure process stability and consistent product quality. The objective of the thesis is the design and experimental validation of a dynamic focusing unit to be integrated in a processing head, capable of automatically compensating for focus variations. For the control scheme to operate in a closed-loop fashion, a feedback signal is generated through the acquisition of the laser beam by a CMOS camera positioned at the end of the optical sensing branch, designed to replicate the power optical path. A dedicated image processing algorithm analyzes the captured beam profile, estimates its dimensions, and adjusts the position of a lens within the optical chain to achieve optimal spot properties. In view of the compactness of the proposed system, a motorized linear stage has been added to the camera to allow for a complete characterization of the laser beam by acquiring cross-section images at various axial positions, which is particularly useful for auto-diagnostic purposes. To this end, efforts have been made to collect measurements for beam caustic and quality factor evaluation. Experimental tests have demonstrated the effectiveness of the system to cope with undesired disturbances, promising for its integration into commercial processing heads as a cost-effective and compact solution offering automatic real-time focus correction.

Contents

List of Figures

List of Tables

Chapter 1

Introduction

Photonics, being the science of the harnessing of light in terms of its generation, detection, and management, has been identified as one of the Key Enabling Technologies, meaning that it is capable of offering a strategic and integrated approach to the development and deployment of new technologies to promote industrial modernization [5], ensuring competitiveness and economic growth. Among the various fields influenced by Photonics, laser manufacturing has proven to be the most significantly impacted.

1.1 Additive manufacturing

At the heart of the Industry 4.0 revolution, whose tendency is towards automation and data exchange in manufacturing technologies and processes, is the concept of additive manufacturing (AM). This term refers to a recent group of techniques that leverage the advantages of rapid prototyping and customized design to obtain complex geometries otherwise difficult or impossible to reproduce with traditional methods (such as molding, casting, machining and more generally each subtracting manufacturing process), allowing the reduction of production time by minimizing both the need for post-processing treatments and the use of additional materials. In this regard, AM processes are characterized by smaller buy-to-fly ratios compared to traditional machining (Figure 1.1 [6]), indicating a more efficient use of materials with a consequent waste reduction (Table 1.1), according to the following definition:

$$\text{Buy-to-Fly ratio} = \frac{\text{Weight of raw material required}}{\text{Weight of finished component}} \tag{1.1}$$

Fabricated parts are made by joining materials, usually layer upon layer, starting from 3D model data [7]. The obtainable accuracy and surface quality depend primarily on the thickness of these layers, each being representative of a cross-section of the designed sample: the thinner they are, the closer the final part will
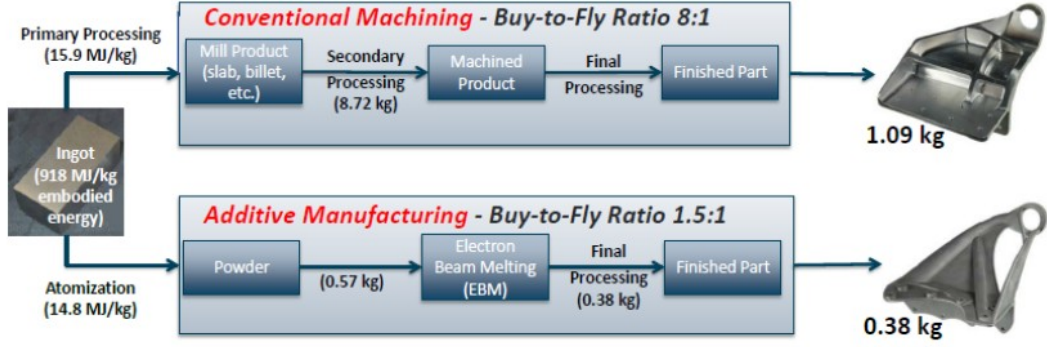
Figure 1.1: Buy-to-Fly ratios of traditional and additive manufacturing.

Table 1.1: Comparison of energy consumption in Machining against AM process.

Process	Final part (kg)	Ingot consumed (kg)	Raw material (MJ)	Manufacturing phase (MJ)	Transport phase (MJ)	Use phase (MJ)	Total energy per bracket (MJ)
Machining	1.09	8.72	8.00	952	41	217.94	**226.945**
Additive manufacturing	0.38	0.57	525	115	14	76.28	**76.937**

be to the original. Although all commercialized AM machines create components in a layer-wise fashion, they differ in (i) the materials used, (ii) the methods by which layers are created, and (iii) the techniques employed to bond them together [8].

The first of these aspects allows for a general distinction between polymer- and metal-based processes. According to the Wohlers' market report [9], as of 2021, the majority of parts were manufactured using polymers (Figure 1.2a), as they constitute a more cost-effective alternative for prototyping, being less dependent on the need for finishing processes.

(a) Materials used in AM.

(b) Metal AM market and forecast [EUR billion].
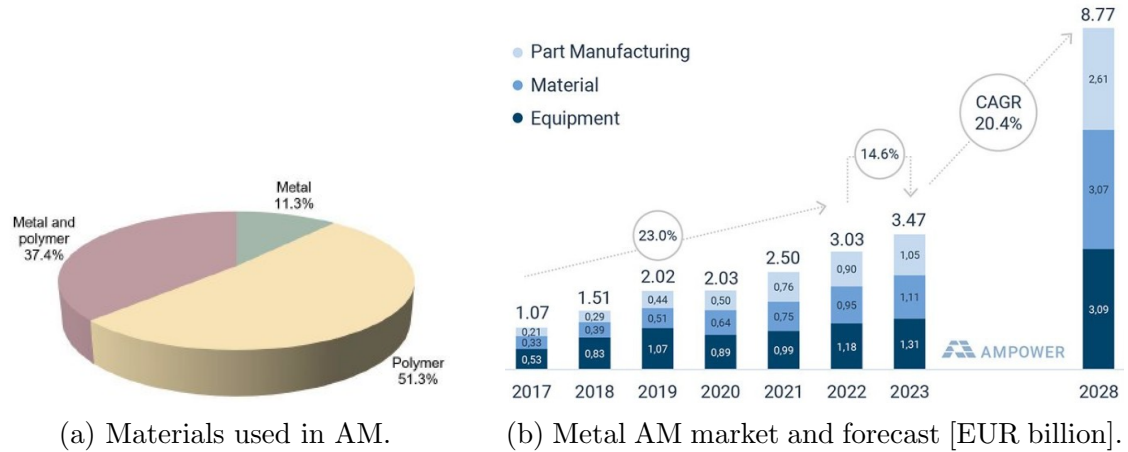
Figure 1.2: Market trends for AM materials and processes.

In contrast, metals provide superior mechanical properties, which makes them more suitable for the production of functional parts. Moreover, the metal AM industry has witnessed an annual growth rate of approximately 15% in 2023, which is expected to increase to around 20% in the next few years (Figure 1.2b [10]): for these reasons, this work focuses specifically on metal AM technologies.

The second and third aspects, namely those regarding the formation and stacking of subsequent layers, allow for a further distinction of AM processes which, according to the normative [7], can be grouped into the following seven categories.

Table 1.2: Classification of AM processes for metals and polymers.

Material	Process						
Metals		Binder Jetting		Powder Bed Fusion (PBF)	Directed Energy Deposition (DED)	Material Extrusion	Sheet Lamination
Polymers	Material Jetting		Vat Photo-polymerization				

In view of the market trends discussed above, the analysis and developments carried out in this work are intended to be applicable to PBF and DED processes. Both techniques are characterized by the use of metal powder as working material, which is melted upon interaction with a laser source.

Depending on the nature of the active medium, being the material providing the optical gain, lasers[1] can be classified as solid state, gas, fiber, or semiconductor. However, the former are increasingly being replaced by waveguide-based systems, as these constitute a more compact alternative, capable of delivering a beam with excellent quality regardless of environmental disturbances [11]. A preliminary indicator of laser performance is the wall-plug efficiency (WPE), which is defined as the fraction of input electrical energy emerging in the laser beam: it gives a measure of energy consumption and operating costs. In the following, each laser type is briefly described and presented in order of increasing efficiency.
For what concern gas media, the CO_2 laser is one of the earliest technologies to have been developed. The lasing action is achieved through vibrational transitions of the gas molecules induced by an electric discharge, resulting in an emission band between 9 and 11 µm, with 10.6 µm being the most common output. This long infrared wavelength is highly absorbed by a wide range of materials, eventually ensuring optimal welding conditions. However, it also imposes limitations on the choice of optical components, since it is also absorbed by ordinary silicate glass, hence requiring special materials. The wall-plug efficiency can be as good as 20%

---

[1]Those relevant in metal AM applications

and high output powers (up to 20 kW) can be achieved, although relatively unstable due to the thermal phenomena generated in the pumping process.

As for fiber lasers, the active medium consists of a rare-earth doped optical fiber, with ytterbium being the most attractive dopant element because of its broad absorption and emission bandwidths, and its flexibility in being pumped at various wavelengths. The wave-guiding nature of these systems ensures several advantages with respect to other types of lasers, including a much higher wall-plug efficiency (up to 40%), increased output power, and superior beam quality. Additionally, the high surface-to-volume ratio of the fiber improves heat dissipation, enhancing robustness to thermal noise.

Semiconductor lasers refer to systems characterized by an active medium typically made of semiconductor compounds, placed inside a resonant optical cavity and driven by an electric current to achieve the lasing condition. Despite being less common in additive manufacturing as primary energy source, laser diodes – particularly in high-power arrays – possess some desirable features which make them attractive for material processing, such as their wall-plug efficiency (around 50%) and their wavelength versatility. In particular, the shorter wavelengths of these lasers enhance absorption in many metals, thereby reducing energy consumption and making them a cost-effective alternative compared to the previous solutions.

Regardless of the energy source utilized, it is critical to understand the laser-powder interaction and how this affects the final properties of the workpiece. The following section addresses this topic with particular attention to the defects that commonly arise in metal AM processes.

1.2   Defects in metal AM processes

Despite PBF and DED have undergone significant technological advancements, the presence of defects remains one of the main challenges limiting mechanical performance and surface finish. Flaw formation can be difficult to predict, as it originates from complex phenomena mainly related to the laser-powder interaction at the melt pool level (such as Marangoni convection, Plateau-Rayleigh effect, spatter, and denudation). Since melt pool behavior has a great impact on the occurrence of flaws, maintaining an optimal laser beam diameter is essential for producing quality parts [12]. Although an in-depth investigation of the relationship between melt pool properties and the resulting defect formation is out of the scope of this thesis (see Grasso et al. [13]), it is anyhow useful to give a general description of the relevant faults that can occur during a process,

Porosity. Also known as void fraction, it is a measure of the "empty" spaces inside the bulk of the fused material. Those voids can be more commonly found either within the layer part or between adjacent layers and, depending on the

physical process responsible for their formation, can be classified as (i) lack of fusion pores, (ii) keyhole pores, and (iii) gas-induced pores. While the first two defects are respectively related to insufficient or excessive energy density at the workpiece, the latter specifically depends on the process under consideration. In PBF, their origin can be due to gas entrapment in the deposited layer; in DED, it can be the consequence of the protective gas breakthrough and injection into the melt pool [14].
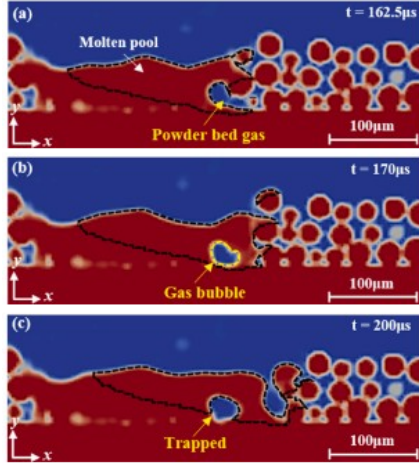
(a) LoF pores mechanism [15].
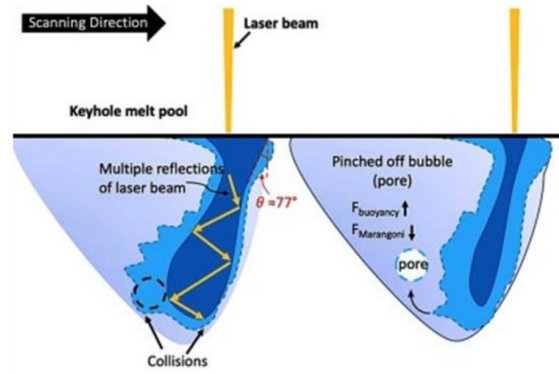
(b) Keyhole pores mechanism.
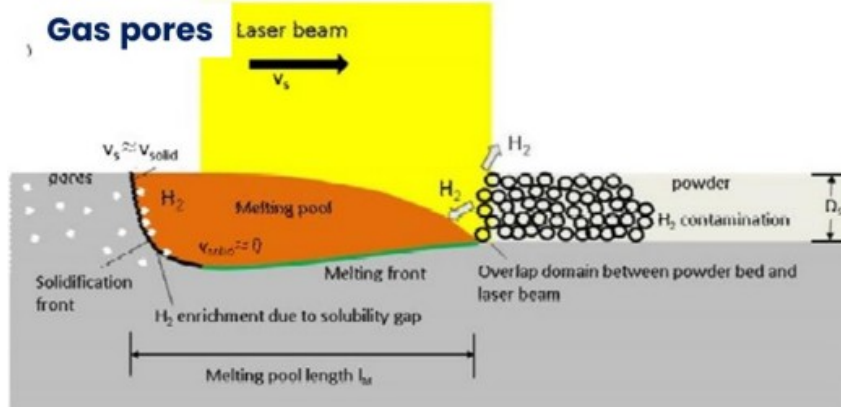
(c) Gas-induced pores mechanism.

Figure 1.3: Main porosity defects.

Residual stresses, cracking and delamination. The complex thermal cycle undergone by the material in a layer-based process causes the formation of thermal gradients, resulting in the build up of tensile stresses which can ultimately lead to cracking phenomena when the ultimate tensile strength is exceeded.

Delamination is a particular case of cracking, occurring when the bonding between subsequent layers is not strong enough to withstand the residual stresses.

(a) Microscopic cracks.   (b) Delamination.
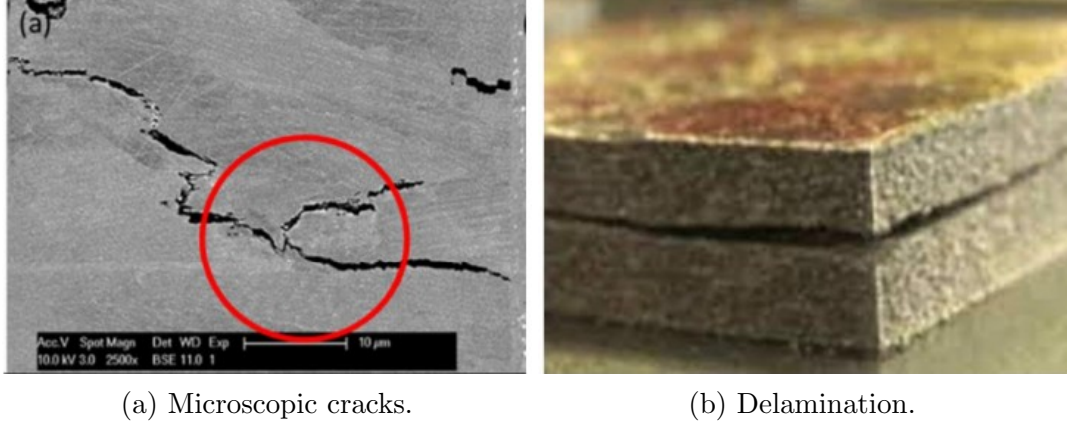
Figure 1.4: Defects induced by residual stresses.

Balling. Improper scanning strategies, such as high scanning speeds or low energy densities, cause the increase of surface tension within the melt pool, which eventually leads to shrinkage of the molten material, resulting in spherical droplets formation during solidification, to the detriment of a homogeneous structure.
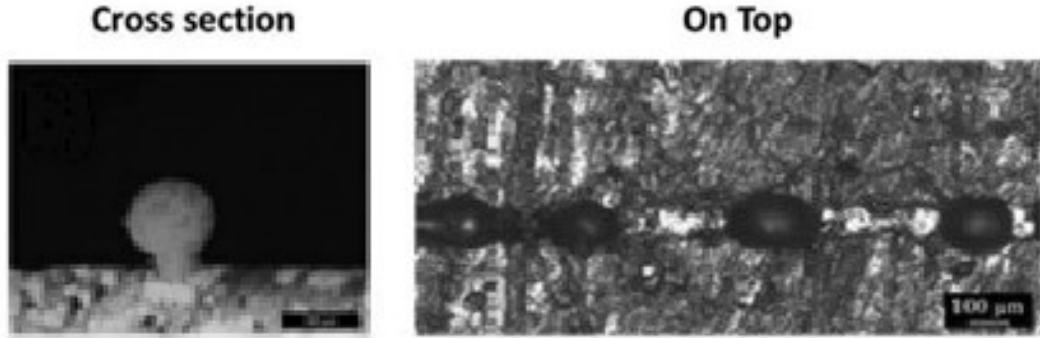
Figure 1.5: Single scan track of balling morphology (on top and cross section micrographs) [1].

Geometric and surface defects. Micro scale phenomena described so far contribute to worsen the macro scale properties of the built model, with geometric and surface properties being the most affected. Geometry deviations include shrinkage and warping (mainly due to residual stresses) when considering the model "as a whole", whereas critical features like thin walls and acute corners

6

may suffer from poor dimensional accuracy (due to the fact that the loose powder surrounding the melt pool in such areas diminishes the heat flux, yielding to local over-heating phenomena). Surface roughness main contributor is the balling effect.
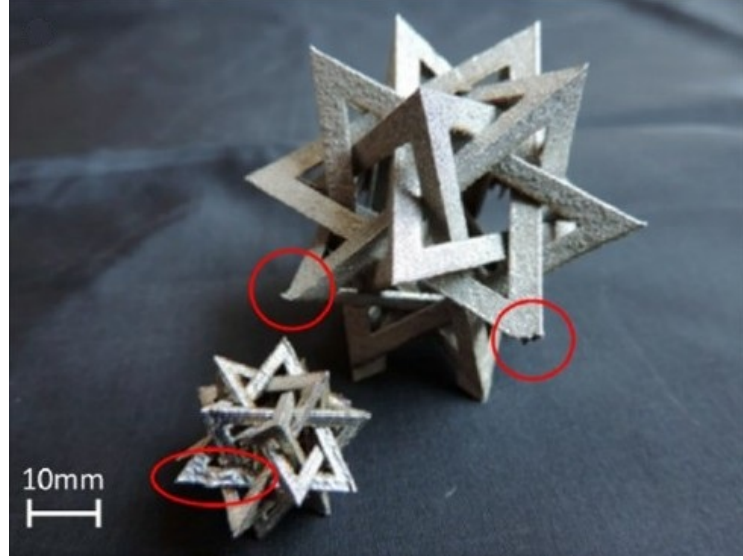
Figure 1.6: Example of geometrical errors in acute corners [2].

By now, the need for a control strategy for beam monitoring and automatic focus adjustment, which has been widely addressed in the literature, becomes evident.

1.3   State-of-the-art on control strategies

Several approaches have been investigated for measuring the critical process signatures, classified on the basis of the sensing method employed for detection as optical-based monitoring, acoustic-based monitoring, and laser line scanning. Novel technologies include the use of X-rays, and multisensor monitoring combined with data fusion. In the present work, attention is drawn to the first type of systems, taken as the starting point in the design and development of the benchtop prototype due to their relative simplicity and the ready availability of the constituting elements.

In practice many processing heads are equipped with monitoring systems based on the detection of back-reflected radiation originating at the laser-powder level and directed to the sensing element through a dichroic mirror (Figure 1.7).

High-speed camera

Lense

Dichroic mirror

Crossjet

Fiberlaser

Collimator

Shifting Lens

X/Y-Mirror

Protective glass

Sheet

Laser radiation
Process radiation
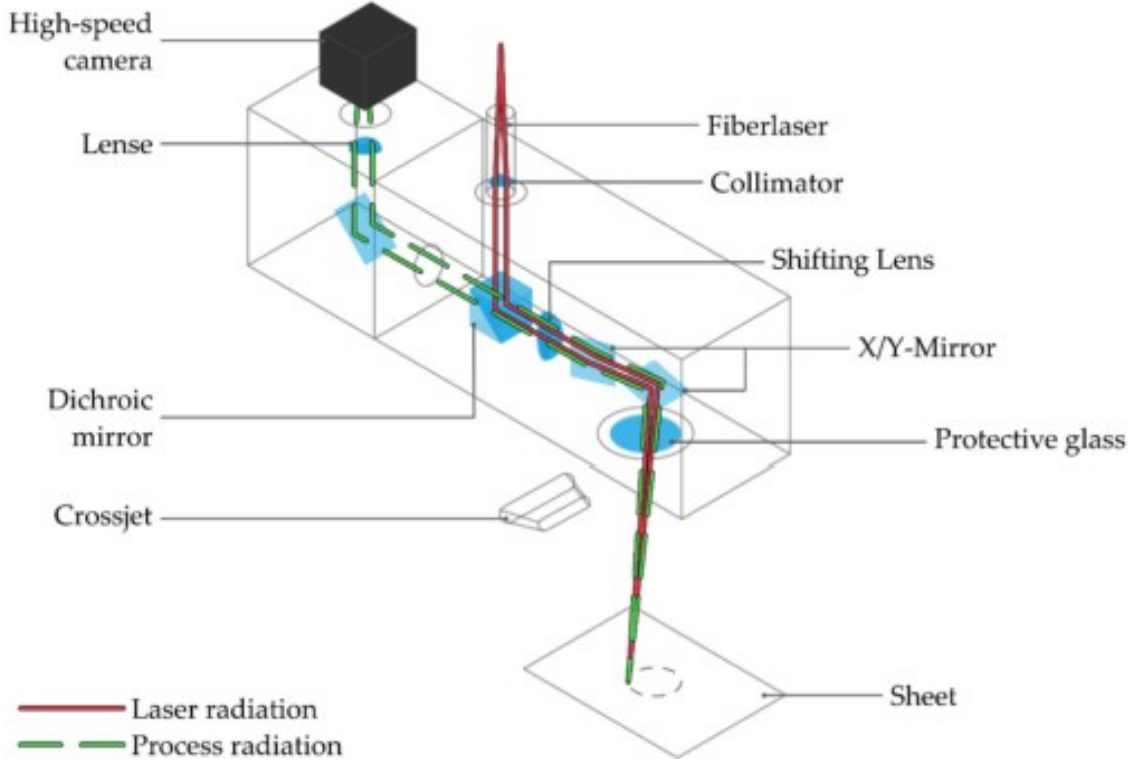
Figure 1.7: Schematic of a processing head with integrated process monitoring capabilities.

Although this solution offers direct process diagnostic and quality control (since the properties of the back-scattered signal are influenced by melt pool dynamics and flaw formation),

Different authors [16, 17] have proposed the use of an off-axial camera configuration which, although simple to install on an already existing AM machine, poses some challenges in correctly determining melt pool dimensions due to oblique viewing angles, thus requiring time-consuming procedures of image pre-processing and calibration. Other studies [18, 19] have focused on the development of a coaxial camera configuration, which guarantees direct viewing capabilities with an improvement in process efficiency. In any case, the image processing phase is carried out to some extent by machine learning algorithms (mainly convolutional neural networks), either to elaborate the acquired images for feature extraction or to correlate such features with the occurrence of defects in the part.

An alternative solution to the use of neural networks is represented by the work of Cao et al. [20], which developed a monitoring system exploiting the reflections of two detecting beams, generated by a unique laser diode directed through a double

hole mask, based on the distance of their spots at the camera sensor. Calibration is required to prevent overlapping of the beams when the working sample is at the focal position of the objective lens (Figure 1.8).

| (a) | (b) | (c) |
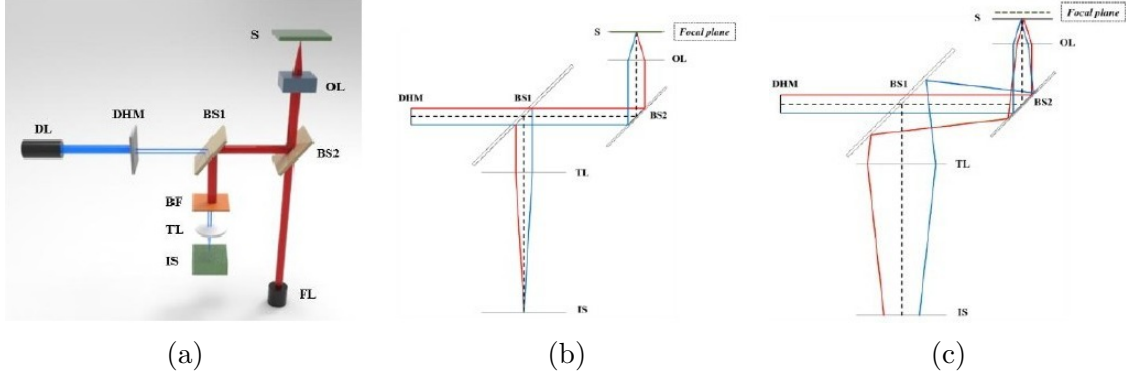
Figure 1.8: Double hole mask system (a) schematic representation, (b) sensing beams with the sample at the focal plane, (c) sensing beams with the sample in front of the focal plane.

Although very attractive, the system described above requires the use of several optical components, which may not be readily available. In addition, the control strategy employed relies on measurements from actual reflections of the laser diodes at the workpiece as it is moved around the focal plane: in the present application the use of a unique beam splitter, characterized by a high split ratio (e.g., 99:1), may be sufficient for considering the reflected beam as representative of the sensing branch.

A simpler optical structure can be achieved by considering the setup presented by Primes GmbH at the Lasers in Manufacturing Conference in 2017 [21], where the laser beam reflections from the protective window are directed through a CCD chip by means of a beam splitter situated behind the focusing lens (see Figure 1.9).
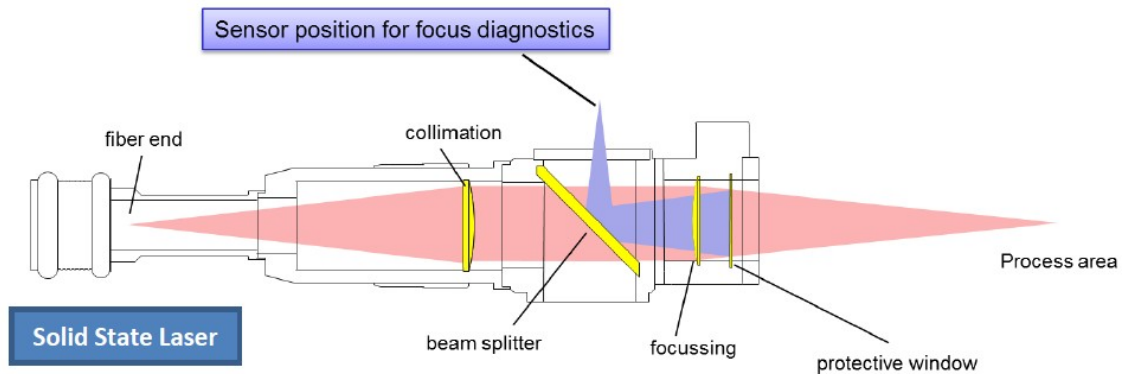
Figure 1.9: Beam monitoring example setup.

Provided that the beam paths from the beam splitter to the focal point of the processing head and to the CCD chip are identical, the image on the CCD chip is a 'twin' of the focal spot. Therefore, a shift in the focal position is registered as a variation in spot size on the CCD chip.

Chapter 2

Theoretical framework

Laser beams exhibit physical characteristics that cannot be accurately described either by plane waves, whose infinite extent in the transverse direction implies carrying an infinite amount of power, or by spherical waves, whose wavefront diverging in all directions could only be generated by an ideal point source. Due to their inherent divergence and spatial confinement, the propagation of laser beams is more accurately characterized by a Gaussian approximation: this model accounts for the finite waist, gradual divergence, and intensity distribution of the beam, offering a mathematically tractable and physically meaningful representation of the beam's behavior in free space.

2.1 Ideal Gaussian beams

The propagation of light is governed by Maxwell's equations. In the absence of free charges and currents, the behavior of the electric field E and magnetic field B can be expressed through the (homogeneous) wave equation. For a monochromatic electromagnetic wave propagating in a homogeneous (independency of medium properties with point position), isotropic (independency of medium properties with field direction) and linear medium, each component of the electric field satisfies the scalar wave equation:

$$\nabla^2 E(\mathbf{r}, t) - \frac{1}{v_{ph}^2} \frac{\partial^2 E(\mathbf{r}, t)}{\partial t^2} = 0 \tag{2.1}$$

where v_{ph} is the speed of light (phase velocity) in a medium with permeability μ and permittivity ϵ.

The assumption of a time-harmonic dependence for the electric field of the following form:

$$E(\mathbf{r}, t) = E(\mathbf{r})e^{-j\omega t} \tag{2.2}$$

and its substitution into Equation 2.1, yields the Helmholtz equation, whose time-independent nature allows to reduce the complexity of the analysis.

$$\nabla^2 E(\mathbf{r}) + k^2 E(\mathbf{r}) = 0 \tag{2.3}$$

To accurately describe Gaussian beam-like solutions, where the wave predominantly propagates along a given axis (commonly the z-axis) and the transverse variation is gradual, the paraxial approximation is introduced. Under this approximation, the envelope of the field amplitude changes slowly along the propagation direction compared to the variation of the oscillating transverse wave: from a mathematical point of view this implies neglecting the second derivative (with respect to z) in $\nabla^2 E(x, y, z)$.

$$\frac{\partial^2 E}{\partial x^2} + \frac{\partial^2 E}{\partial y^2} - 2jk\frac{\partial E}{\partial z} = 0 \tag{2.4}$$

The solution to Eq. 2.4 is the ideal Gaussian beam (Fig. 2.1), which represents a particular type of electromagnetic radiation whose transverse electric field distribution at any axial position is described by a Gaussian function. Identifying the radial position in the transverse plane as $r = \sqrt{x^2 + y^2}$, the complex electric field in phasor notation is given by:

$$E(r, z) = \underbrace{E_0}_{\text{Const.}} \underbrace{\frac{w_0}{w(z)}}_{\substack{\text{Contraction} \\ \text{ratio}}} \underbrace{\exp\left(-\frac{r^2}{w^2(z)}\right)}_{\substack{\text{Transverse} \\ \text{amplitude} \\ \text{distribution}}} \underbrace{\exp\left(-j\left(kz + k\frac{r^2}{2R(z)} - \psi(z)\right)\right)}_{\text{Spherical wavefront}} \tag{2.5}$$
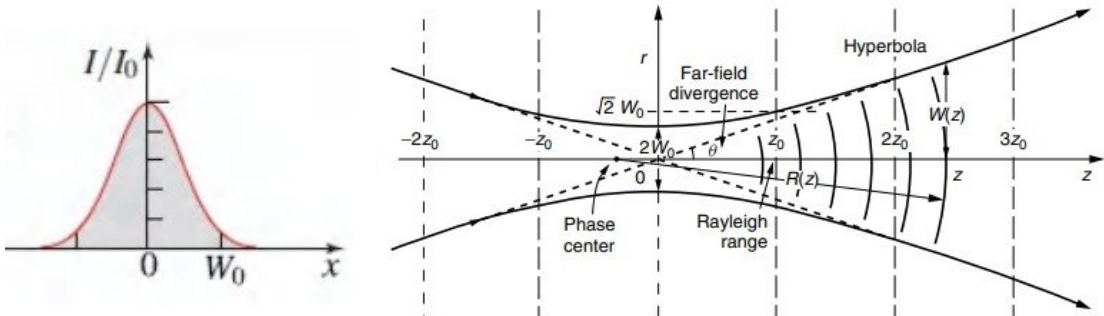
Figure 2.1: Gaussian beam normalized intensity at $z = 0$ (left) and amplitude distribution (right).

The first three terms characterize the field amplitude and its variation along both the longitudinal (contraction ratio) and the transverse (transverse-amplitude distribution) direction. The result of this variation is represented in Figure 2.2 in terms of intensity: at each transverse section, the intensity distribution $I(r, z = z^*)$ has its maximum on the beam axis, while the longitudinal intensity distribution $I(0, z)$ has its maximum at $z = 0$. The last exponential accounts for phase correction terms.
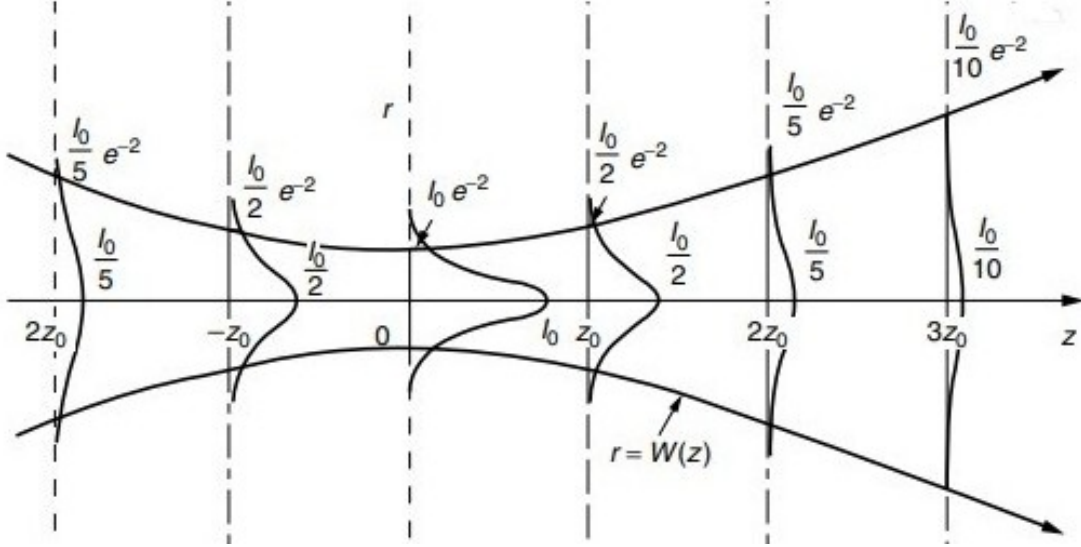
Figure 2.2: Gaussian beam cross section intensity.

With reference to Equation 2.5, the main parameters describing the propagation and evolution of a Gaussian beam are:

- the beam width or beam radius $w(z)$, defined as the radial distance (from an on-axis point) at which the intensity drops to $1/e^2$ of its axial value. Its dependence on the longitudinal distance z is governed by:

$$w(z) = w_0 \sqrt{1 + \left(\frac{z}{z_R}\right)^2} \tag{2.6}$$

The minimum value w_0, which occurs at $z = 0$, is known as the waist radius.

- the Rayleigh length z_R, defined as the distance from the waist at which the width of the beam is $\sqrt{2}$ times its minimum value. Physically speaking, it marks the boundary between the near-field region, where the beam wavefront is approximately planar, and the far-field region, where divergence becomes

more significant. It is determined, given the beam's waist size, as:

$$z_R = \frac{\pi w_0^2 n}{\lambda_0} \tag{2.7}$$

- the divergence angle θ, which is a measure of how fast the beam expands in the far field. In this region, the beam radius increases linearly, allowing the definition of the half-angle as:

$$\theta = \lim_{z \to \infty} \frac{w(z)}{z} \overset{\text{paraxial case}}{=} \frac{\lambda}{\pi w_0} \tag{2.8}$$

- the radius of curvature $R(z)$, which characterizes the curvature of the beam's wavefront. It can be computed according to the following equation:

$$R(z) = z \left[1 + \left(\frac{z_R}{z} \right)^2 \right] \tag{2.9}$$

- the Gouy phase ψ, which corresponds to an excess delay of the beam's wavefront in relation to a plane wave, particularly relevant in the near-field:

$$\psi(z) = \arctan \left(\frac{z}{z_R} \right) \tag{2.10}$$

Provided that the peak amplitude E_0 in Equation 2.5 and the wavelength λ are known, an ideal Gaussian beam can be fully characterized by two parameters: the location of its waist and one of either the Rayleigh range z_R or the waist radius w_0.

2.2   Real Gaussian beams

Ideal Gaussian beams described so far are characterized by a transverse field pattern known as the fundamental (or TEM_{00}) mode, whose desirable features − including the lowest possible divergence (for a given beam waist and wavelength) and the capability to be focused to the smallest achievable spot size − highlight their diffraction-limited nature.

In practice, imperfections in the laser source and other perturbations give rise to the excitation of higher-order transverse modes (solutions to Equation 2.4 where a spatial dependency on x and y is assumed for the field's amplitude), which cause the beam's intensity profile to deviate from the ideal Gaussian shape. It follows that the definition of a real Gaussian beam requires the introduction of two additional parameters related to the quality of the laser source (although only one of them is sufficient for their full characterization).

A first evaluation of the beam "composition" is provided by the Beam Parameter Product (BPP), which is defined as the product of the beam waist radius w_0 and the far-field half-angle divergence θ and is thus measured in $mm \cdot mrad$.

$$\text{BPP} = w_0 \cdot \theta \tag{2.11}$$

The smallest possible value for the BPP is that of an ideal Gaussian beam, which at a given wavelength is:

$$\text{BPP}_{\text{id}} = \frac{\lambda}{\pi} \tag{2.12}$$

Alternatively, beam's quality degradation can be quantified by the introduction of a quality factor M^2. It is a wavelength-independent parameter defined as the ratio of the BPP of the actual beam to that of a corresponding ideal Gaussian.

$$M^2 = \frac{w_{0R} \cdot \theta_R}{w_0 \cdot \theta_0} \tag{2.13}$$

The higher the M^2 value, the worse is the quality of the beam (meaning a greater deviation from the ideal case): the lowest possible value, corresponding to a perfect Gaussian profile, is $M^2 = 1$.

The propagation characteristics of realistic beams are modified by this quality factor, whose interpretation depends on the parameter that the multimode beam and a reference Gaussian beam have in common. In particular, they can be seen to have:

- matching waists ($w_{0R} = w_0$), in which case the value of M^2 represents how much the real beam diverges compared to the pure Gaussian.

$$\theta_{0R} = M^2 \theta_0 \tag{2.14}$$

- matching divergences ($\theta_{0R} = \theta_0$), in which case the value of M^2 represents how much larger the real beam waist is with respect to the pure Gaussian beam waist.

$$w_{0R} = M^2 w_0 \tag{2.15}$$

- matching Rayleigh range ($z_{RR} = z_{R0}$), in which case the real beam is studied in terms of an equivalent model having a waist and a divergence $\sqrt{M^2}$ times larger than that of the reference Embedded Gaussian (represented for convenience in Figure 2.3). The propagation equations can therefore be expressed as:

$$w_R(z) = w_{0R} \sqrt{\left[1 + \left(\frac{z \lambda M^2}{\pi w_{0R}^2} \right)^2 \right]} \tag{2.16}$$

and:

15

$$R_R(z) = z \left[1 + \left(\frac{\pi w_{0R}^2}{z \lambda M^2} \right)^2 \right] \tag{2.17}$$
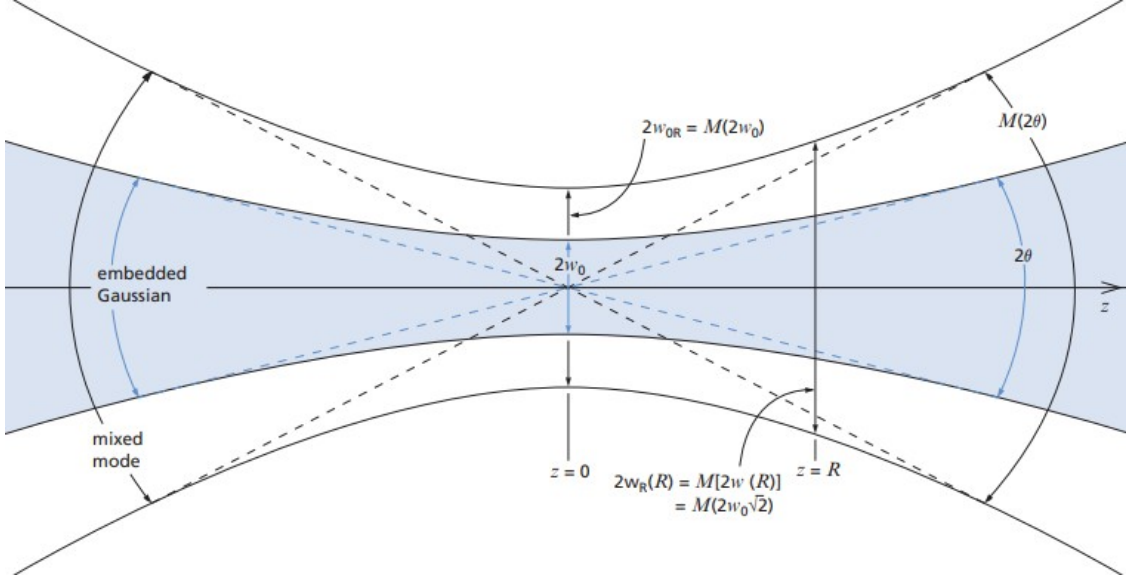
Figure 2.3: Embedded Gaussian (in blue) and mixed-mode beam sharing the same Rayleigh distance.

2.3 Optical components

When designing an optical system, a suitable combination of optical components must be chosen to manipulate an incoming light beam to meet certain specific requirements. These elements are indeed designed to control and modify the propagation of light according to some physical phenomena: among them, perhaps the most widespread devices are lenses, pieces of glass shaped by two opposing surfaces which exploit the principle of refraction to produce converging or diverging light rays, in accordance with Snell's law.

$$n_1 \sin \theta_1 = n_2 \sin \theta_2 \tag{2.18}$$

A preliminary classification of lenses can be made based on geometric considerations of their surfaces. The most common category is that of spherical lenses, where each surface is a part of a sphere and, therefore, possesses the same radius of curvature in two orthogonal planes. In addition to these, other types of lenses include cylindrical, aspherical, and toric lenses, each characterized by having different radii

of curvature along two orthogonal directions on a given surface.

A further classification can be made based on their optical behavior, which depends on the geometry of the lens as well as on the relative orientation between the normal to its surfaces and the incident light rays:

- positive lenses cause convergence of a collimated beam (traveling parallel to the optical axis) towards a spot on the axis, at a distance called focal length;

- negative lenses cause divergence of a collimated beam (traveling parallel to the optical axis), which appears to be emanating from a particular point on the axis, at a distance called focal length.
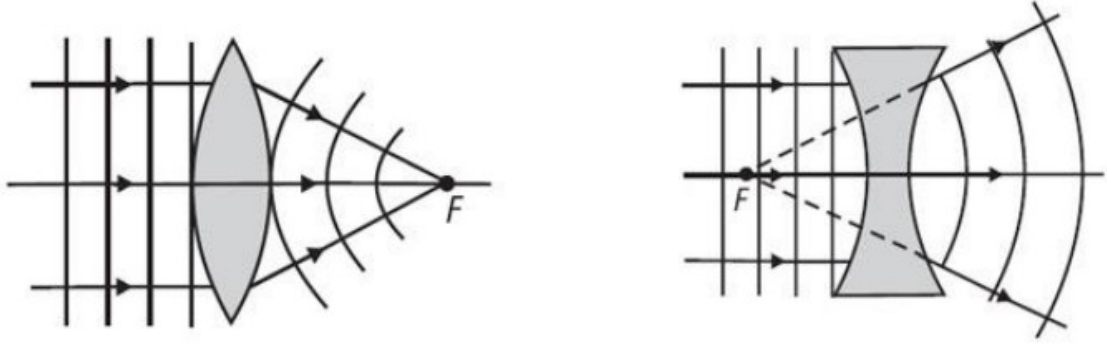
Figure 2.4: Parallel rays focused by a positive lens (left) and diverged by a negative lens (right).

Moreover, depending on the orientation of its normal $\hat{\mathbf{n}}$, the surface of a lens can be defined as convex ($\hat{\mathbf{n}} > 0$, pointing outward) or concave ($\hat{\mathbf{n}} < 0$, pointing inward).

A comprehensive description of a lens requires the definition of its main parameters (see Figure 2.5):

- D, diameter of the lens.

- R_1, radius of curvature, defined as the radius of the sphere whose center of curvature is located along the optical axis.

- EFL (Effective Focal Length), defined as the distance from a principal plane of the lens to its imaging plane.

- BFL (Back Focal Length), defined as the distance between the last surface of the lens to its imaging plane.

- P'', being the hypothetical plane where incident light rays can be considered to bend due to refraction and known as the principal plane.

- CT, center thickness, defined as the physical separation between the two surfaces measured along the optical axis.
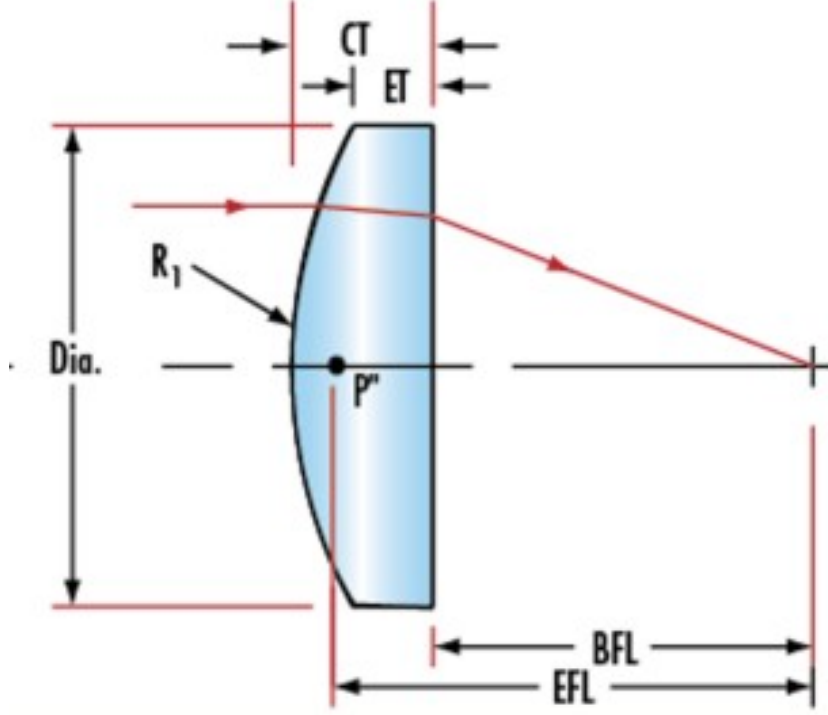
Figure 2.5: Main parameters of a (plano-convex) lens.

One of the most useful concepts in the design and improvement of an optical system is the size and placement of the system's aperture stop, which is the opening in the lens assembly that limits the amount of transmitted light. For a single lens, this coincides with the clear aperture, or effective diameter, and allows the definition of another parameter, known as the Numerical Aperture (NA), expressing the light-gathering capability of the element. The NA depends on the sine of the angle made by the marginal ray (directed from an on-axis point to the edge of the aperture stop) with the optical axis and on the refractive index of the medium surrounding the lens.

$$NA = n\sin\theta = n\sin\left[\arctan\left(\frac{D}{2 \cdot EFL}\right)\right] \overset{\overset{\text{usually, n=1}}{\downarrow}}{\approx} \frac{D}{2 \cdot EFL} \qquad (2.19)$$

To the extent that a lens fails to produce perfect images, deviations from ideal performance − causing a detriment of image quality and compromising beam focusing accuracy − are a measure of the optical errors, or aberrations, in the lens. The presence of these imperfections depends on the incident location of an incoming light ray and can be understood by using Seidel's expansion of aberrations in terms of the odd-order products $h^a\rho^b$ of normalized entrance ray location ρ and object height h: the lowest-order $(a+b=3)$ nontrivial terms are the five (monochromatic) aberrations reported in Table 2.1.

Table 2.1: Aberrations and ρ-h dependency.

Aberration	ρ-h **dependence**
Spherical aberration	ρ^3
Coma	$\rho^2 h$
Astigmatism (tangential)	$\rho_y h^2$
Astigmatism (sagittal)	$\rho_x h^2$
Petzval curvature	ρh^2
Distortion	h^3

Perhaps the main type of aberration due to its influence on the cone of light originating from an on-axis point, is spherical aberration (SA), which causes rays parallel to the optical axis to converge to different points, resulting in a bright spot surrounded by a faint halo (Figure 2.6). The effects of SA can be quantified in terms of:

- longitudinal spherical aberration; it is the distance along the optical axis of the intercept of paraxial rays and marginal rays.

- transverse spherical aberration; it is the height at which marginal rays intercept the paraxial focal plane.
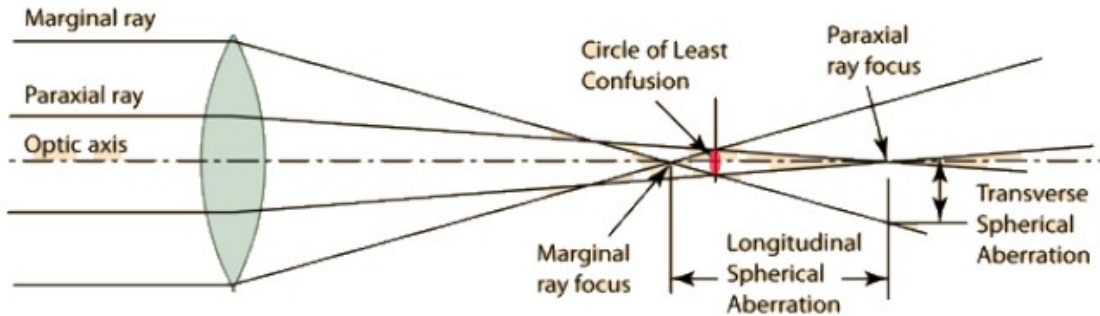
Figure 2.6: Effects of spherical aberration.

19

Spherical aberration depends on lens shape, orientation, and conjugate ratio and can be minimized by using suitably designed singlets, whose shape is called best-form: for low-index glasses at infinite conjugate this is a lens with different radius of curvature on the two sides, although in practice plano-convex with curved side toward the infinite conjugate are used, as they perform nearly as well as the best-form lenses (see Figure 2.7).
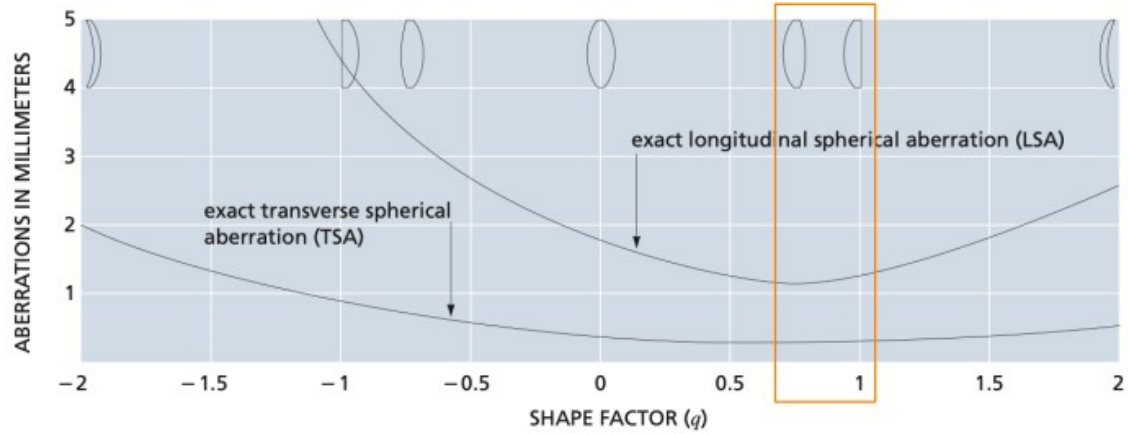
Figure 2.7: Aberrations of specific positive singlets at infinite conjugate ratio as a function of shape.

Chapter 3

System definition

The developed system, having to compensate for focus variations on the basis of acquired images from a camera, inherits the structure from classical closed-loop architectures, even though the reference signal is not constant and indeed corresponds to the most recent measured beam dimension, since the control action is based on a gradient descent-like algorithm. In this framework, the plant corresponds to the optical chain of the dynamic focusing unit, the actuator can be seen as the motorized linear stage, and the sensing block can be identified with the CMOS camera sensor.

3.1 Design of the optical chain

The preliminary step involved in the design of the lens arrangement required to correctly propagate the beam is the definition of the energy source to be used. This consists of a commercial module belonging to the nLIGHT® alta™ Fiber Lasers family, featuring an output power – at 10 V analog input – of approximately 1 kW and characterized by the following optical properties.

Table 3.1: Datasheet of the nLIGHT® 1 kW module.

Optical property	Unit	Value
Beam Parameter Product	mm · mrad	1.00
Nominal Core diameter	µm	50
Divergence	mrad	51.0
Wavelength Centroid	nm	1068.7

With reference to Table 3.1, knowing the divergence (which is intended as the half-angle) and the BPP, it is possible to calculate the waist radius inverting Equation 2.11, resulting in a value of $w_0 = 19.6\,\mu m$. In addition, the knowledge of the BPP

and of the operating wavelength allows for the calculation of the M^2 value according to Equation 2.13, yielding a result of $M^2 = 2.9$.

As for the simulation, this is carried out starting from an open-source Python code, properly modified to account for real beam propagation. The choice to operate in such an environment is motivated by its high integration capabilities, allowing the script to be run on a micro-controller, and by the good correspondence with the results obtained using a commercial software (see Appendix A for more details). The preliminary considerations regarding the choice of the lenses to be used were based on simulations performed using ideal thin lenses, although real commercial lenses are represented in the figures for graphical purposes. The simulation has been later refined to account for real components and actual distances. As will be evident in Chapter 4, the higher spot sizes observed in the real setup suggested a revision of the initially proposed configuration.

Before diving into the analysis, it is necessary to define the desired properties of the outgoing beam, mainly in terms of waist radius (spot size) at the focal position: since there are no stringent requirements regarding its minimum and maximum values, the optical elements have been chosen so as to obtain a beam diameter of approximately $100\,\mu$m at a distance of $150\,$mm from the protecting window of the processing head, as these are considered reasonable parameters for many PBF applications. That being sad, the optical chain consists of four lenses, which serve the functions of collimation, beam expansion, and focalization. The use of a beam expander doublet allows for higher precision in the execution of the focus compensation task without altering the beam's optical path, which would occur if the focusing lens were to be moved instead. In the following sections, each element is briefly presented, with particular attention to its effects on beam propagation characteristics.

3.1.1   Collimating lens

Collimation refers to the process of minimizing the divergence (ideally reducing it to 0) of incoming light rays, preventing the beam from spreading as it propagates. Although recommended, this operation must be performed whenever the beam exhibits high divergence or when the optical path includes movable elements, whose movement requires the geometrical properties of the beam to remain constant.

The main aspect to consider when choosing a collimating lens is to ensure that the incoming light source is entirely accepted by the optical element. This imposes a limit on the minimum allowable numerical aperture of the lens, which must be greater than that of the laser beam.

$$\text{NA}_{\text{Lens}} > \text{NA}_{\text{Laser}} \sim \sin 0.051 = 0.051 \tag{3.1}$$

As expected, due to the low divergence of the employed source, Equation 3.1 does not represent a severe constraint and nearly any lens could be used for collimation. However, the need to initially operate at low power led to the use of the aiming laser integrated in the nLIGHT$^{\circledR}$ module – a red pointer emitted by a diode and thus characterized by a higher divergence. Furthermore, as can be seen in Figure 3.1, improving the collimation of an extended source characterized by a given height requires the use of lenses with longer focal lengths, although this compromises the numerical aperture.

$$\text{Divergence} \approx \frac{\text{Size of the Source}}{\text{Focal Length of the Collimating Lens}} = \frac{y_1}{f} \qquad (3.2)$$

In practice, due to the limited size of the source, small output divergences are obtained regardless of the focal length (see Figure 3.1[1]), meaning that Equation 3.2 does not significantly constrain the design choices.
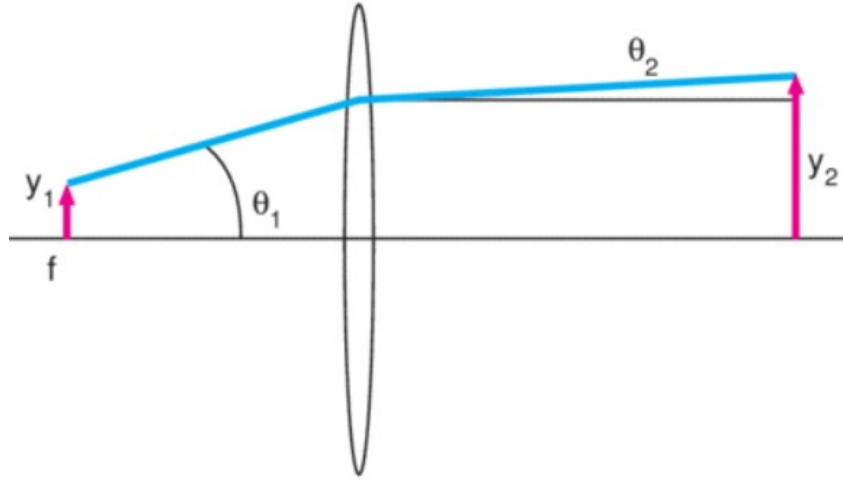
Figure 3.1: Collimation of an extended source [3].

At this stage, the main limiting factor in the choice of a collimating lens is represented by the physical distance between the emitting point and the output surface of the module, measured to be 14 mm. This constraint ultimately suggested the use of a 25 mm effective focal length (as this corresponds to the minimum allowable back focal length, being the reference position at which the flat surface of the lens must be placed relative to the light source). As can be seen in Figure 3.2, showing the simulation result involving the propagation of the infrared source, the given

---

[1]The notation has been inherited from image formation analyses, with y being representative of the beam waist radius

lens is expected to properly collect the output coming from a laser diode, since it is characterized by a numerical aperture that exceeds the values typically associated with such energy sources.
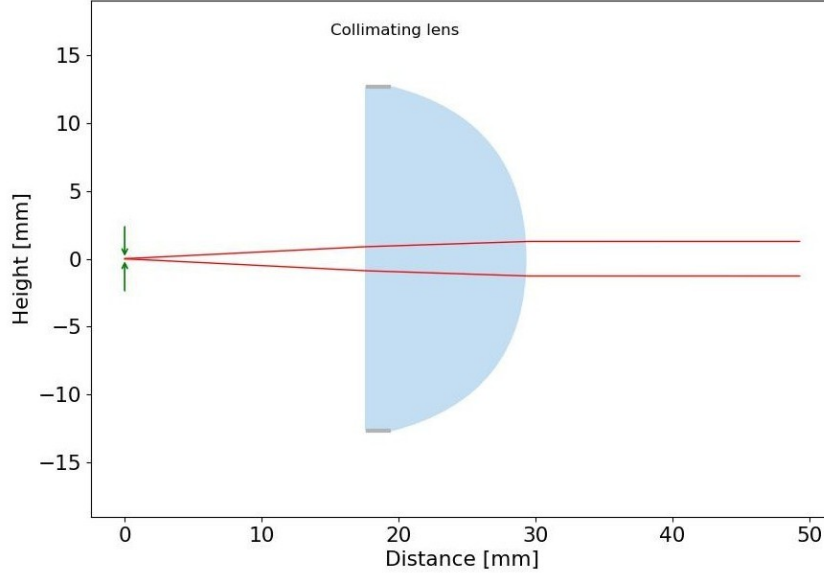
Figure 3.2: Beam propagation through a collimating lens.

3.1.2 Beam expander

As already anticipated, the need to have a movable element within the optical chain, through which focus compensation can be performed, leads to the adoption of a beam expander – an optical device that expands the width of a collimated beam at its input. The expansion is achieved by means of two elements that, in the case of the Galilean design, consist of a negative lens, causing the input beam to diverge, followed by a positive lens, responsible for collimation (Figure 3.3).

The proposed solution is well suited for high-power applications because of the absence of a real focus between the lenses. By virtue of the invariance of the BPP, it is possible to quantify the magnification by introducing the beam expansion ratio:

$$m_{12} = -\frac{f_2}{f_1} \tag{3.3}$$

with $f_2 > 0$ and $f_1 < 0$ being the focal lengths of the convex and concave lens, respectively. Equation 3.3 holds provided that the two lenses are separated by a distance equal to the difference of their focal lengths $f_2 - |f_1|$.
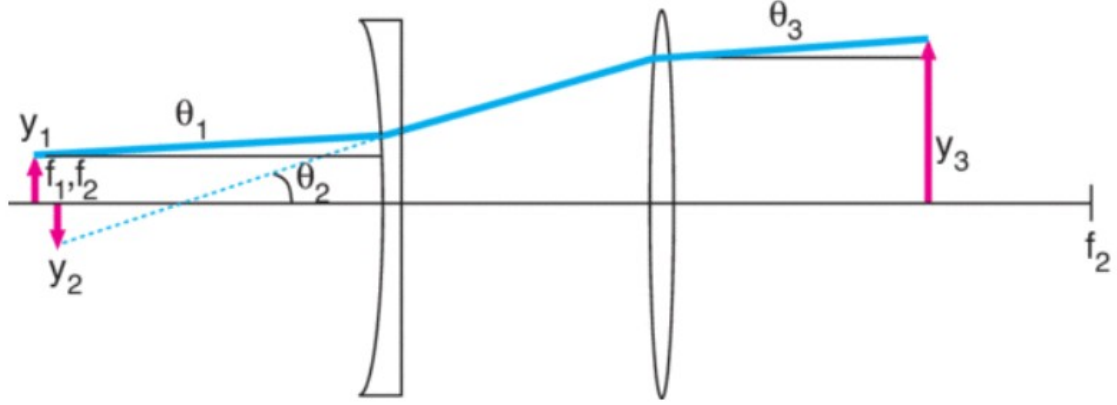
Figure 3.3: Laser beam expansion.

For the present application, having a lower expansion ratio may be beneficial to avoid excessive spreading of the beam, whose greater diameter at the focusing length results in lower spot sizes which, although desirable for material processing, are difficult to be analyzed with the imaging software. Hence, a magnification of $m_{12} = 2$ has been chosen, which has been obtained having set the focal lengths at $f_1 = -30\,\mathrm{mm}$ and $f_2 = 60\,\mathrm{mm}$ (Figure 3.4).
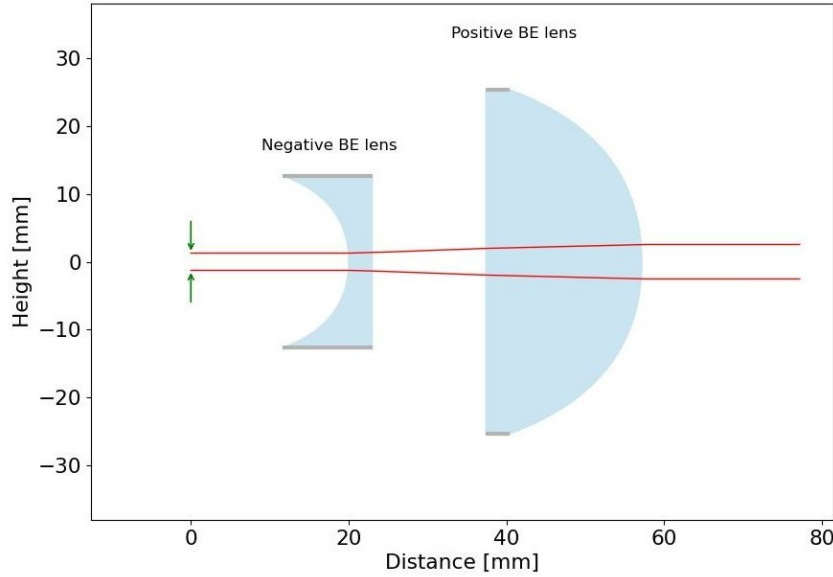
Figure 3.4: Beam propagation through a beam expander.

3.1.3 Focusing lens

The design of the focusing lens mainly involves the choice of a suitable focal length, which must satisfy conflicting requirements. On one hand, it should be as low as possible to reduce the spot size at the focal plane, as can be seen in Figure 3.1 by reversing the direction of light propagation, where the height of the focused beam is given by $y_1 = f \cdot \theta_2$. However, this could impose being too close to the workpiece. In addition, greater spot sizes resulting from longer focal lengths can be more easily detected at the camera sensor, as was previously observed.

Eventually, a focal length of 150 mm has been selected, as this was considered a reasonable compromise between maintaining a proper working distance and ensuring detectable spot size variations.
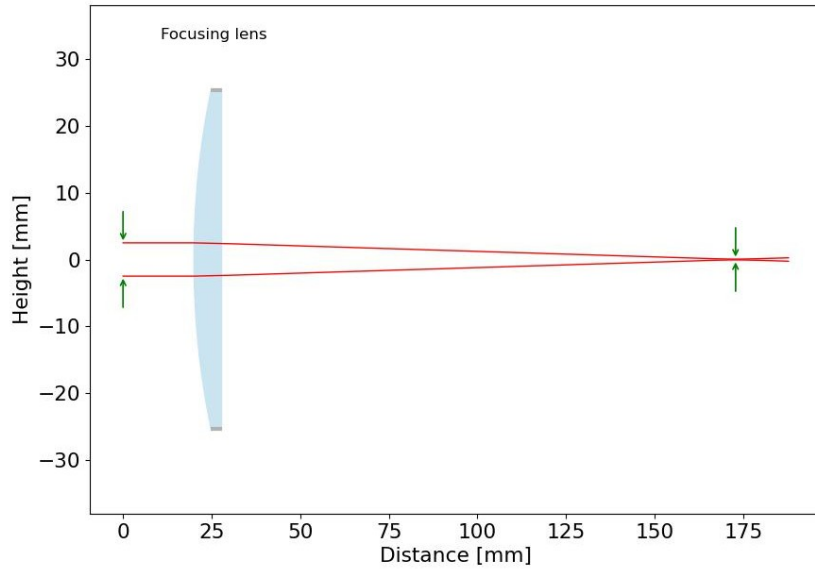
Figure 3.5: Beam propagation through a focusing lens.

3.2 Beam sensing and detection

As discussed previously, the feedback signal is generated upon interaction of the laser beam with the sensor of a CMOS camera, positioned at the focal plane of the focusing lens and constituting the sensing branch of the system, which is conceptually similar to that illustrated in Figure 1.8. The beam spot has been detected by means of the IDS UI-1220SE-M-GL Rev.2 camera (Figure 3.6a), initially validated by measuring the dimensions of a known object suitably illuminated. The element that served this scope is a Thorlabs fiber adapter plate (Figure 3.6b), whose clear

aperture is stated to be equal to 3.2 mm.

(a) CMOS camera for beam detection.

(b) SM1SMA Fiber Adapter Plate.

Figure 3.6: Components employed for the camera validation setup.

The light source has been provided simply by a small portable torch, and the resulting image is shown in Figure 3.7, where the `Measure` function of the uEye Cockpit software has been used to estimate the object's dimension, yielding a value of 533 pixels. Given that each pixel has a specified size of 6 µm, the measurement obtained from the camera is in agreement with the real physical size of the object.

3.3 Motorized linear stage for lens positioning

The lens repositioning actuation task is performed by means of a motorized linear stage, belonging to the Zaber X-LSQ family (Figure 3.8). These devices are well-suited for automatic control applications, owing to their extensive programmability within a Python environment via the `Zaber Motion Library`, which provides a comprehensive set of commands for motion control and device configuration.
The programming instructions are executed upon powering on the linear stage and establishing a connection with the computer: all the relevant classes are found inside the `zaber_motion.ascii` sub-module, which refers to the protocol used for communication between the two devices. The preliminary step before moving the device, is to enable such connection as reported below.

```python
from zaber_motion.ascii import Connection

# Opening a connection
with Connection.open_serial_port("COM3") as connection:
```
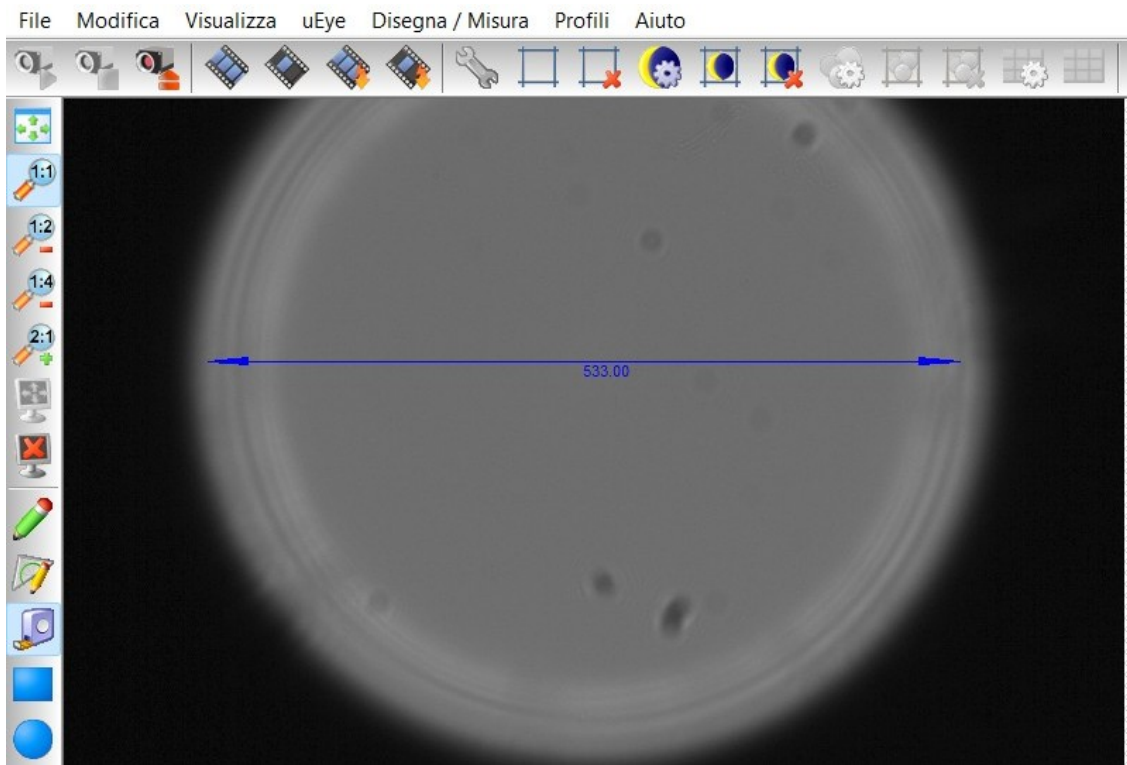
Figure 3.7: Camera validation result.

Figure 3.8: Zaber X-LSQ150D linear stage.

```
5    connection.enable_alerts()
6
```

```
7      # Detect devices
8      device_list = connection.detect_devices()
9      print("Found {} devices".format(len(device_list)))
10
11     device = device_list[0]
```

Listing 3.1: Simple connection example

Perhaps the most important feature is the `Axis` class, which allows for specifying the movement of the guide and retrieving information about its status.

```
13     from zaber_motion import Units
14
15     # Get the axis of the device
16     axis = device.get_axis(1)
17
18     # Homming the device
19     if not axis.is_homed():
20         axis.home()
21
22     # Move to 50mm
23     axis.move_absolute(50, Units.LENGTH_MILLIMETRES)
24
25     # Move by an additional 1mm
26     axis.move_relative(1, Units.LENGTH_MILLIMETRES)
```

Listing 3.2: Simple connection example (cont.)

Chapter 4

Experimental setup and results

Having demonstrated the possibility of compensating for focus variations with the chosen lens sequence, an experimental prototype has been assembled to test the effectiveness of the developed control algorithm.

4.1 Assembly of the optical chain

The optical chain has been assembled by fixing each lens separately by means of suitable mounts from Thorlabs, as those reported in Figure 4.1 for the 2 inch lenses. This choice, although requiring much effort to achieve the correct alignment and centering, is motivated by the need to have a movable element that limits the use of a cage system.

(a) LCP34T/M - 60 mm Cage Plate.　　　(b) Precision Kinematic Mount KS2.

Figure 4.1: Lens mounts to hold the elements in place.

As far as the negative lens is concerned, this is anchored to the guide exploiting a right-angle connection between posts achieved through a suitable angle clamp (Figure 4.2a).

(a) RA90/M Angle Clamp. (b) CP35 - 30 mm Cage Plate.
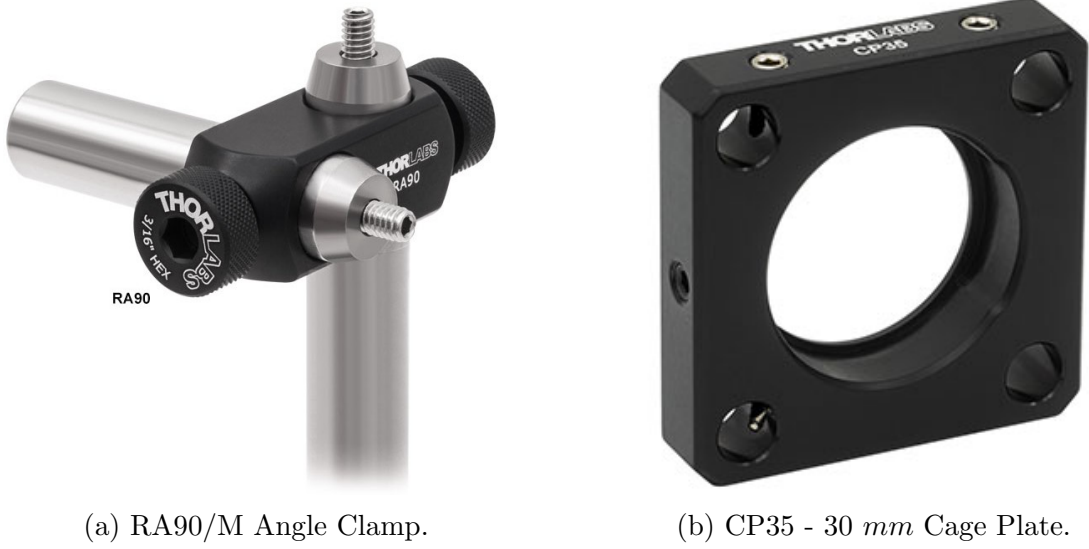
Figure 4.2: Configuration to secure the negative lens to the guide.

The adopted configuration allows the reduction of the overall longitudinal dimension of the system, which is also limited by the physical available size of the optical table. Similar reasoning can be done when fixing the camera.

As already pointed out, the alignment of the chain is not a trivial task and it has been performed with the aid of the CMOS camera, which has been used to check the resulting beam dimension after the insertion of each element. This procedure was particularly useful for checking whether proper collimation was obtained. Besides the collimating lens, the chosen optics consists of UV fused silica lenses, because of the excellent thermomechanical properties of this material, which makes it suitable for high-power applications.

A notable difference with respect to the simulation carried out in Section 3.1 is the replacement of the positive lens in the beam expander with the focusing lens. The result is the obtainment of a greater expansion ratio and a shorter focal length, the latter being beneficial for M^2 measurements: the resulting smaller spot size implies a higher divergence and a shorter Rayleigh range. The assembled prototype can be seen in Figure 4.3.
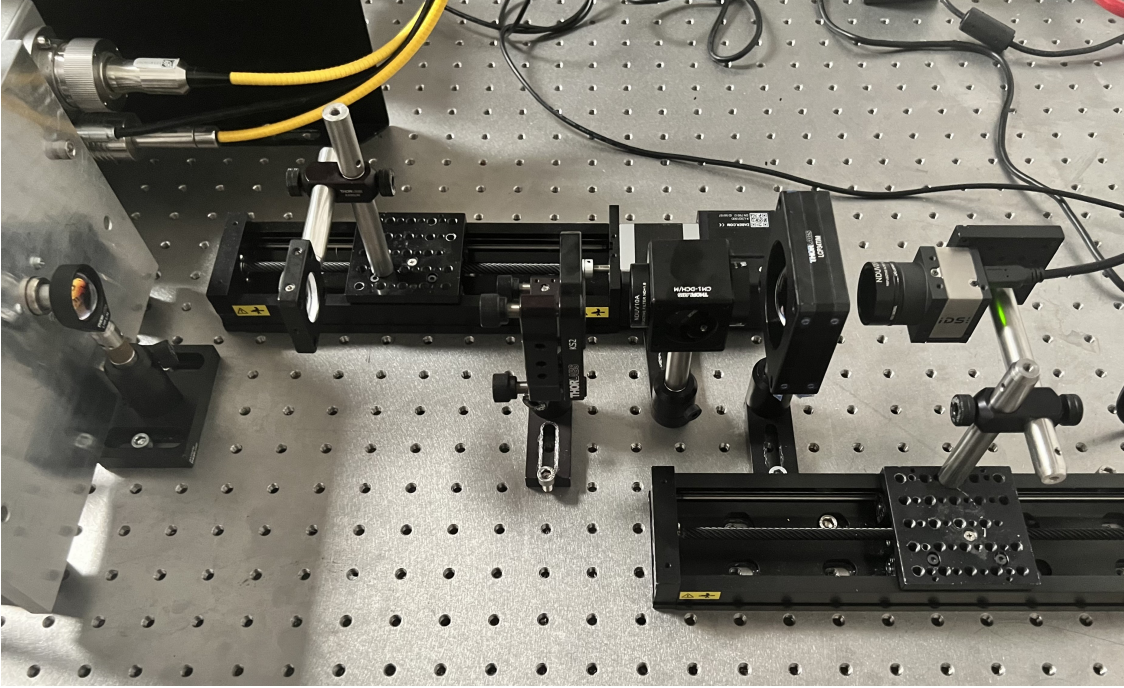
Figure 4.3: Assembly of the dynamic focusing system.

Once again, it should be noted that the proposed setup is intended to represent only the sensing branch of the system. Additionally, the presence of filters [1] was considered fundamental in trying to reduce the incident optical power at the camera sensor which, even in the low-power scenario, can take on values causing the image to saturate and hence hindering correct beam measurements. What may happen in presence of saturation is that the Python-based script for beam dimension computation, being reliant on counting pixels depending on their intensity (and whose working principle is given in Appendix B), can consider in the definition of the diameter the tails of the transverse Gaussian distribution, which are usually discarded being representative of points whose intensity falls below $1/e^2$ of the maximum value. Eventually, the filters have been placed along the optical path in a non-consecutive arrangement to minimize multiple reflections occurring at their interfaces, which ultimately result in the formation of additional bright spots at the camera sensor, thereby perturbing the measuring process.

---

[1]In total, three reflective filters have been used: two $ND20$ and one $ND10$. The term ND stands for neutral density and indicates the attenuation factor introduced by the filter, expressed on a logarithmic scale.

4.2   Evaluation of automatic focus control

Before the dynamic focusing task can actually start, the movable lens must be positioned at the optimal distance required to achieve proper collimation at the output of the beam expander. This alignment procedure is particularly necessary the first time the system is operated, due to the homing sequence performed by the linear stage to establish its reference position. The lens positioning algorithm is implemented through an iterative procedure with the use of a `while` loop where, at each iteration, the guide is moved by a specific predefined amount along a direction which is updated depending on the detected beam size at the camera sensor: if the relative difference between the current and the previous measured diameters is larger than a selected threshold, the direction of motion is inverted and halved. The decision to employ an optimization-like algorithm lies in the fact that, at the desired lens position (i.e., when its distance with respect to the positive lens of the beam expander is equal to the difference of focal lengths) and with the sensor kept fixed, the measured spot size reaches its minimum value. Care should be taken in choosing an appropriate step size ensuring a detectable difference between two consecutive measurements. Instead of running the code starting from the home position, as this would require several iterations to converge to the desired solution, the lens is initially moved to an arbitrary position, corresponding to half the stroke of the guide (that is, $75\,\mathrm{mm}$).

Once the lens reaches the optimal position, the automatic focus control action is executed by continuously updating the current spot size and comparing it to the value corresponding to the previous iteration: whenever their difference exceeds the threshold, the liner stage is moved to search for the new optimal position, following the same procedure used for the initial lens alignment. To trigger a variation in the measured beam diameter and hence simulating a shift of the focal plane, the camera has been manually moved from its starting location. Although the system reacts quickly to camera movements, the time required to displace the lens can be relatively long – on the order of tens of seconds – which, depending on the application, may not be considered acceptable (for instance, if the aim of the focus compensation scheme is to maintain a flat working surface in response to a beam being rapidly deflected across various positions). However, if the purpose is that of compensating thermal lensing effects, which are sustained as long as the heating condition persists, then the resulting delay needed to settle in response to an input focus variation can be considered acceptable and beneficial.

During the test procedure, a Python script has been implemented for the creation of a file to record the initial and final beam dimensions (before and after camera movement), the time required for lens repositioning, and the value of the newly determined optimal position. Regrettably, the latter measurement proved to be

unreliable in many tests, as the guide lost its reference position while the code was running. The lens and the camera are initially placed at 76 mm and 203 mm on their respective linear stages. The results obtained when the camera is moved to 204 mm and 200 mm are reported below.

Table 4.1: Results of the dynamic focusing task.

Camera position [mm]	Lens position [mm]	Previous_dx [μm]	Previous_dy [μm]	Current_dx [μm]	Current_dy [μm]	Time [s]
203.00	76.03	164.05	158.47	164.05	158.47	-
→ 204.00	→ 82.91	304.05	289.73	148.03	142.58	16.2
← 200.00	← 60.78	917.92	696.13	150.58	144.86	39.5

With reference to Table 4.1, `Previous_dx` and `Previous_dy` refer to the measured diameters acquired at the beginning of the dynamic focusing task and hence with the camera shifted with respect to the original position. Analogously, `Current_dx` and `Current_dy` are the spot sizes detected once the lens has settled to the newly computed optimal position.

The validation of the system is performed by direct comparison with a simulation carried out in Zemax: despite the motivations which justified the use of an open-source script to perform the design phase, the advanced modeling capabilities and enhanced reliability of a commercial software are preferred to confirm the outcomes of experimental tests. Starting from the setup discussed in Appendix A, the Zemax built-in optimizing feature has been exploited to find the relative distance between the beam expander lenses needed to produce the desired focus shift. This has been done by changing the position of the focal plane and optimizing according to the `PARY` operand, which has been set to have a 0 paraxial ray height as target value at the reference surface. The initial lens spacing of 112.5 mm, corresponding to the stage position of 76.03 mm, results in a paraxial focal plane located 49.58 mm away from the last lens surface: by relatively moving 1 mm forward and 3 mm backward (to simulate the same working conditions of the real system), the following results are obtained.

Table 4.2: Results of the simulated dynamic focusing task.

Paraxial focal plane location [mm]	Relative displacement [mm]	Relative distance between BE lenses [mm]	Expected position of the linear stage [mm]
48.58	−1	118.27	81.80
49.58	0	112.50	76.03
52.58	+3	97.02	60.55

As can be seen by comparing the expected position of the linear stage (fourth column of Table 4.2) with the actual attained position (second column of Table 4.1), the developed algorithm displace the negative lens with a relative error smaller

than 5%, which can be considered totally acceptable for the present application.

4.3 Measurements of beam quality factor

Quality factor measurements are taken with the negative lens back to the original optimal position. The camera is moved around the focal plane, corresponding to an absolute position of 204 mm of the second linear stage, by relative steps of 0.25 mm and 1 mm depending on whether the measured diameters fall, respectively, within one Rayleigh length or beyond two Rayleigh lengths. These values have been determined by a trial-and-error procedure, which may not be acceptable for real-time beam diagnostic applications: a possible improvement could involve obtaining a rough estimate of the Rayleigh range based on the measured beam waist. At each axial position, the size of the beam is extracted, and its diameters along the principal axes are stored in arrays which are then used for M^2 fitting. The result of the operation is shown in Figure 4.4, having considered only the 'horizontal' direction.
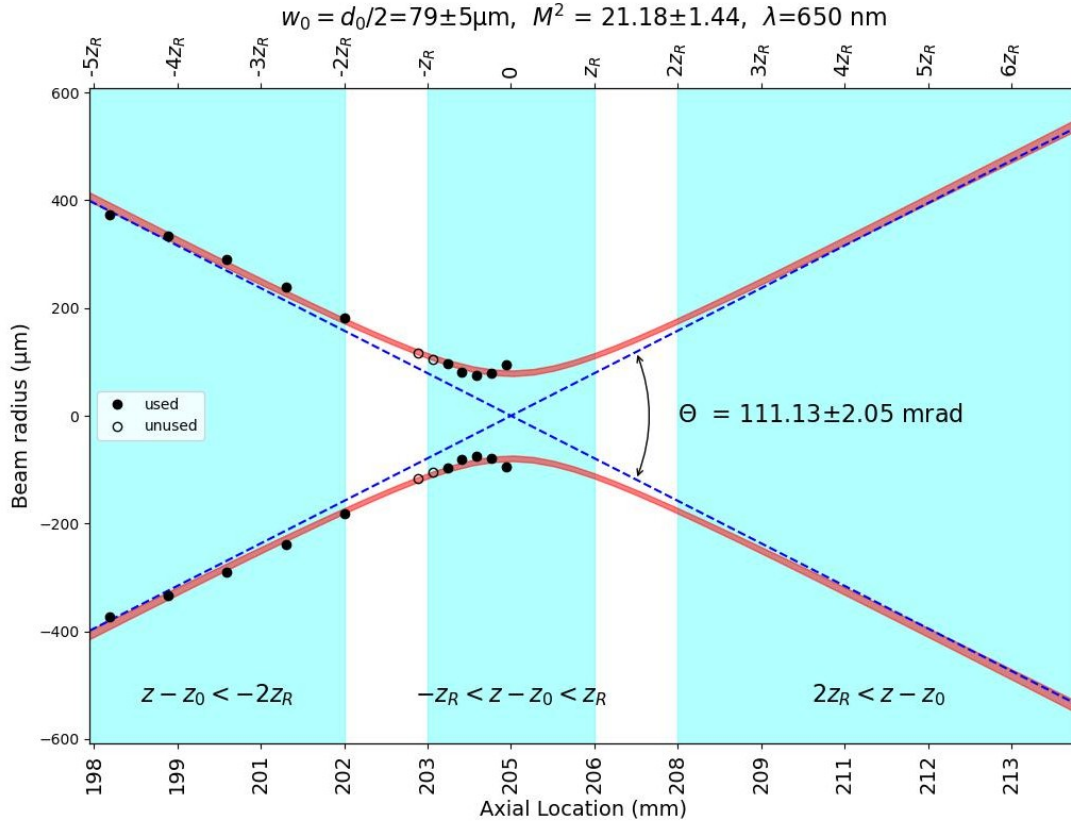

Figure 4.4: M^2 fitting from measured beam diameters.

A meaningful interpretation of the obtained M^2 can only be given upon validating the software tool through the analysis of a known source (further details are given at the end of Appendix B). Although a reasonable fit of the data points has been obtained, the resulting quality factor appears somewhat high given the employed laser source. In particular, the red pointer is expected to exhibit an M^2 value comparable to that of the high-power module. A possible reason for this mismatch is that the acquired images near the focal position highly saturate (Figure 4.5) despite the presence of the filters, eventually resulting in the possibility of overestimating the dimension of the spot: since in this framework the actual beam and the reference Gaussian share the same waist, the bigger this is and the smaller will be the divergence of the reference beam, thereby worsening the quality factor.
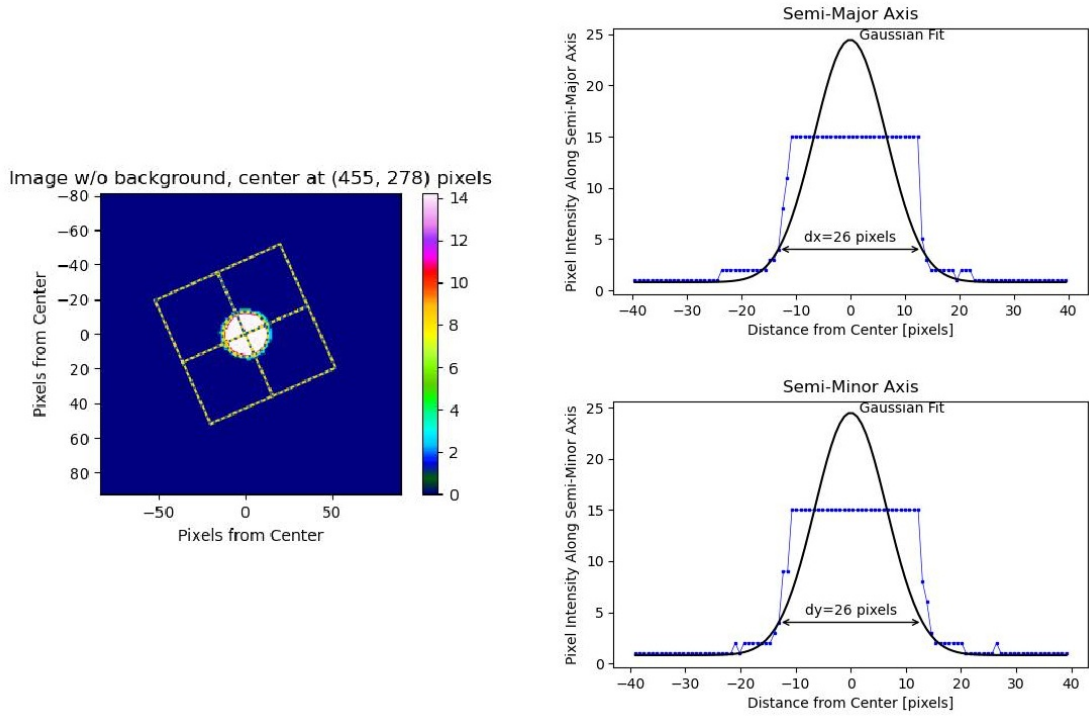

Figure 4.5: Example of image saturation (left) and Gaussian fit of the measured data (right).

A 99 : 1 beam splitter could be inserted within the optical chain oriented such that 1% of the incident power is transmitted to the image sensor. This would help prevent saturation, given that the exposure time of the camera has already been set to its minimum value.

Chapter 5

Conclusions

The work carried out in this thesis laid the foundations for the development of a system dedicated to laser beam characterization and dynamic focus adjustment. Particular attention has been drawn to the integration of optical and mechanical components, and to the implementation of a control strategy based on image acquisition and beam size computation, carried out through dedicated software tools. The results obtained from the experimental tests pave the way for further improvements and hold promise for the realization of a functional prototype.

5.1 Results overview

The experimental tests confirmed the correct operation of the system. To verify whether the lens was properly repositioned in response to the movement of the camera, the code has been interrupted, and the lens has been manually moved in the vicinity of the computed optimal position, revealing that the attained location effectively corresponded to the minimum spot size, validating the effectiveness of the implemented adjustment strategy. As far as the beam quality factor is concerned, the M^2 measurement values did not seem to fully align with the expected characteristics of the source. However, it should be noted that complete information regarding the source specifications were not available, and moreover, the beam quality may have deteriorated over time.

Overall, the proposed setup for dynamic focus adjustment and quality factor evaluation could have been further improved by a more precise alignment and positioning of the elements within the optical chain, as well as by the use of specific components, not available at that time in the Alite facility, which would have been beneficial in trying to reduce the optical intensity delivered at the camera sensor.

5.2 Future developments

As already anticipated, several aspects remain open for improvement and development, involving both the physical layout of the optical chain and the software routines responsible for image acquisition, beam size computation, and focus adjustment. From the optical design perspective, the adoption of a zoom optical system could be conceived as an alternative to the current beam expander. Thanks to its internal lens arrangement (Figure 5.1), a zoom optics is capable of modifying the effective focal length and magnification while maintaining beam collimation, possibly offering enhanced performance in the execution of the dynamic focusing task provided that a suitable relationship is found linking the measured diameter with the occurrence of focal shift and that a focusing lens is added at the rear end of the afocal system to form an image.

From the software standpoint, key areas for improvement include the optimization of the implemented control strategy, with the aim of achieving faster convergence to the

Figure 5.1: Movement of lenses in an afocal zoom system.

result, and the refinement of the beam size computation algorithm, whose current accuracy remains limited. Alternatively, the use of a higher resolution image sensor could be explored to enhance measurement precision. Furthermore, the development of an auto-exposure adjustment routine could prove useful, especially when acquiring images far from the focal position: in these regions, the lower optical intensity of the beam prevents pixel saturation, allowing the exposure time to be increased for improved spot detection. Eventually, the image acquisition task could be integrated with segmentation techniques, which are particularly useful whenever the image contains artifacts, such as additional spots caused by unwanted reflections.
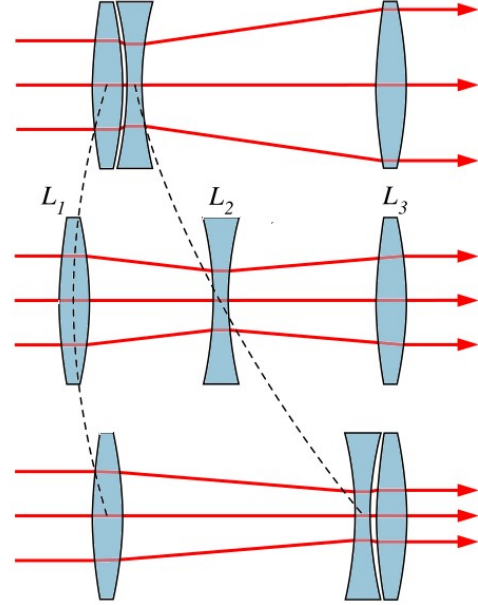
Appendix A

Ray tracing techniques

In the context of the thesis work, it is of paramount importance the use of software tools to aid the design procedure by means of simulations of the optical system. Zemax® is a powerful alternative as far as the prediction of the behavior of the system is considered, but may constitute a limitation when it comes to communicating with a micro-controller to perform some control actions. In this regard, the open-source ray tracing software may constitute a valid option to deal with the aforementioned programming «issues», as it makes use of a python environment. For this reason, its characteristics and theoretical foundations will be addressed in the following sections.

A.1 Gaussian beam propagation

The open-source software works under the assumption of paraxial behavior, meaning that the rays form small angles with respect to the optical axis. In this way, the ABCD matrices describing the elements of the system and allowing ray tracing appear without trigonometric dependencies, making the computations easier.
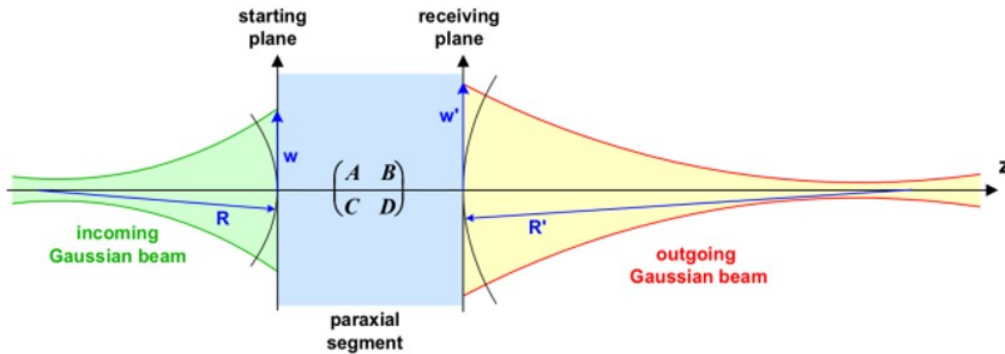

Figure A.1: Gaussian beam propagation through a paraxial system

The Python module constitutes a useful tool for calculating various properties of optical paths, being it well-suited for both image formation analysis. The matrix formalism allows to deal with propagation of ideal Gaussian beams (Figure A.1), upon definition of the beam complex parameter q, whose reciprocal carries information about the radius of curvature and Rayleigh range, respectively related with its real and imaginary parts. An alternative definition of the q parameter can be given, knowing the axial position z, according to:

$$q(z) = z + j\frac{\pi w_0^2}{\lambda} = z + jz_R \tag{A.1}$$

Given the initial parameter q_{in} and provided that the ray transfer matrix of the system is known, the output properties of the beam after propagation are given by:
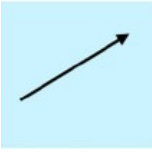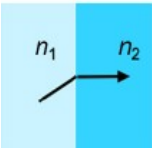
$$q_{out} = \frac{Aq_{in} + B}{Cq_{in} + D} \tag{A.2}$$

Taking advantage of object-oriented programming, the module groups elements into classes, with *Matrix*, *MatrixGroup*, *GaussianBeam*, and *LaserPath* being the most relevant for the present application.

A.1.1 *Matrix* and *MatrixGroup* classes

Both classes define the main optical elements of a system, with the only difference that `MatrixGroup` can be used to group `Matrix` elements together. Their substantial equivalence makes it possible to exploit the class inheritance mechanism, whereby a child class acquires all the methods and attributes of its parent class (`Matrix` in this case), which will be the focus of our attention.

An element can be inserted directly by specifying its ABCD matrix entries and several additional parameters such as its physical length. Alternatively, it is possible to resort to other subclasses depending on the type of element to be used: a comprehensive classification along with the related matrices is given in Table A.1.

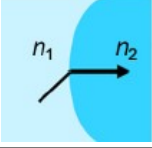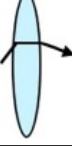|		
	$\begin{bmatrix} 1 & d \\ 0 & 1 \end{bmatrix}$	Free-Space Propagation with an Arbitrary Distance of d
	$\begin{bmatrix} 1 & 0 \\ 0 & \frac{n_1}{n_2} \end{bmatrix}$	Refraction at a Planar Boundary n_1 and n_2

|		
	$\begin{bmatrix} 1 & 0 \\ -\frac{n_2-n_1}{n_2 R} & \frac{n_1}{n_2} \end{bmatrix}$	Refraction at a Spherical Boundary n_1 and n_2, with $R > 0$ for a Convex Boundary
	$\begin{bmatrix} 1 & 0 \\ -\frac{1}{f} & 1 \end{bmatrix}$	Transmission through a Thin Lens with Focal Length $f > 0$ for convex

Table A.1: ABCD matrices of different optical elements within the paraxial approximation [4].

A.1.2 *GaussianBeam* class

The `GaussianBeam` object can be defined either by directly specifying the complex q parameter (in terms of real and imaginary parts) or by providing the beam size w and the radius of curvature R, along with the working wavelength and the refractive index through which the beam propagates: the result is essentially the same, as these parameters contribute to the definition of q. Originally, the module did not account for the behavior of real beams; this feature has been introduced by suitably modifying the propagation equations (as in Eqs 2.16 and 2.17) to include the beam quality factor M^2. The reference theoretical framework is that of the embedded Gaussian described in Section 2.2.


```
9   # Define the initial Gaussian beam (real)
10  w0r = 0.05
11  M2 = 80
12  w0 = w0r/sqrt(M2)
13
14  B1 = GaussianBeam(w=w0, n=1)
15
16
17  B_r = GaussianBeam(w=w0r, n=1, M2 = 80)
18  print(B_r, B1)
19
20  beams = [B1, B_r]
21
22  # Define an arbitrary path through which propagate the beam
23  path = LaserPath()
24  path.append(Space(d=15))
25  path.display(beams)
26
27  B1_out = path.mul_beam(B1)
28  B_r_out = path.mul_beam(B_r)
29
30  print(B1_out, B_r_out)
31
32  th1 = B1_out.w/B1_out.z
33  thr = B_r_out.w/B_r_out.z
34
35  BPP = B1_out.wavelength/math.pi
36
37  print(B_r.w0/B1.w0)
38  print(thr/th1)
```
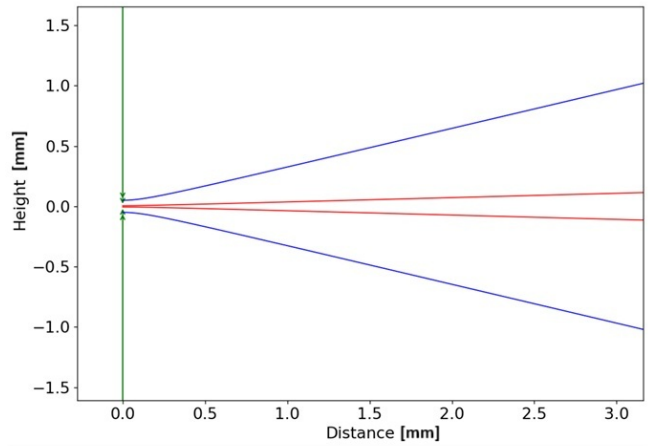
The ratio of real waist size to embedded waist size is: 8.944271909999157
The ratio of real divergence to embedded divergence is: 8.94427190999916

Figure A.2: Comparison between real beam (in blue) and embedded Gaussian (in red) propagation.

A.1.3 *LaserPath* class

As far as the propagation environment of the beam is concerned, this is built starting from a `LaserPath` object which, being essentially a subclass of `MatrixGroup`, inherits the ability to create the optical path by cascading single elements through the `append()` method.

A.2 Open-source software validation

To check whether the results obtained with the Python module can be considered reasonable, it is worth showing a simulation example of a Galilean beam expander whose outcome is compared against two commercial software. Particular attention is given to the shift of focal position caused by a change in the relative distance between the lenses composing the system.

The code implements a `for` loop where, after each iteration, the entire optical path is redefined with the modified distances. As can be seen in Figure A.3, where the comparison is performed with respect to MATLAB®, there is little to no difference between the results (as expected, since in both cases the calculations are performed using beam-matrix multiplication).
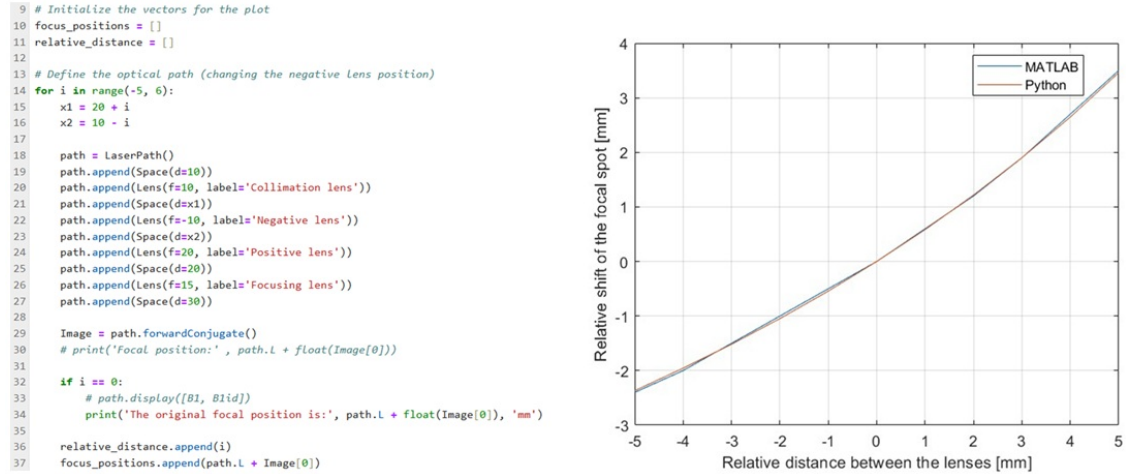
Figure A.3: Portion of the code in Python environment (left) and comparison of the result with the one obtained in MATLAB® (right).

Eventually, a comparison is made with respect to Zemax®. The code is the same as in the previous case, with the only difference being that the lenses are now specified as the commercial lenses from Thorlabs actually employed in the construction of the optical chain and the distances are taken from real physical measurements of

the system. The comparison result is shown in Figure A.4: this time the differences are more pronounced because the commercial software does not rely on simple ray transfer matrix analysis. Nevertheless, this discrepancy can be considered acceptable for the purposes of the present work.
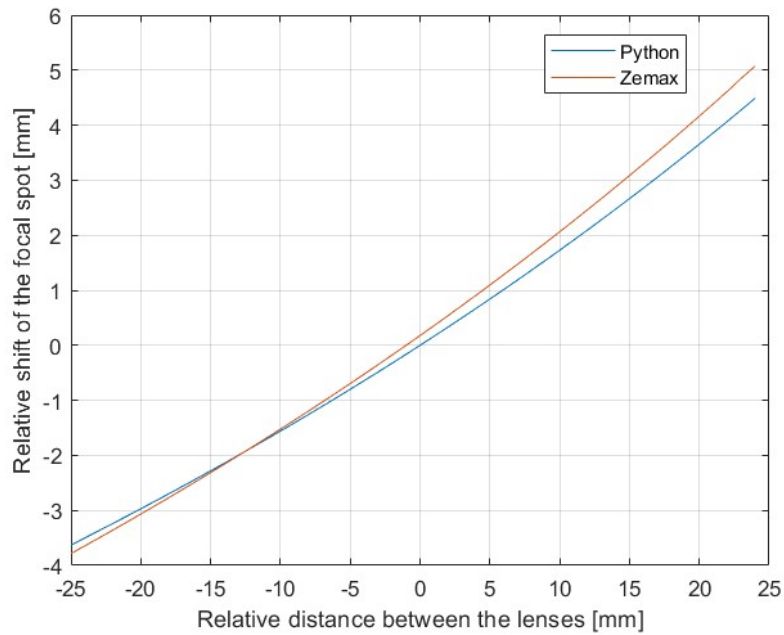

Figure A.4: Comparison of the open-source result with the one obtained in Zemax® OpticStudio.

Appendix B

Software tools for laser beam analysis

The working principle of the feedback signal generation relies on image acquisition followed by software-based processing to extract the geometrical properties of the laser beam. The algorithm, whose theoretical background refers to the `ISO 11146-2` normative, leverages the work by Scott Prahl [22].

B.1 Beam size computation

In this framework, the description of the laser beam is ascribed to the second-order moments of the Wigner distribution, which gives the amount of power – at an axial location z – passing through the lateral positions (x, y) with given paraxial angles (θ_x, θ_y) to the z axis. The integration of the Wigner distribution over the angles leads to the definition of the power density distribution $E(x, y)$, which can be further integrated over the lateral positions, yielding to the total power of the beam.

$$P = \int_{-\infty}^{+\infty} \int_{-\infty}^{+\infty} E(x, y) \, dx \, dy \tag{B.1}$$

The center of the beam is given by the first-order moments of the distribution, which can be directly obtained from the power density as:

$$\langle x \rangle = x_c = \frac{1}{P} \int_{-\infty}^{+\infty} \int_{-\infty}^{+\infty} x E(x, y) \, dx \, dy \tag{B.2}$$

and

$$\langle y \rangle = y_c = \frac{1}{P} \int_{-\infty}^{+\infty} \int_{-\infty}^{+\infty} y E(x, y) \, dx \, dy \tag{B.3}$$

The parameters characterizing the extent of a general two-dimensional distribution $E(x, y)$ are the variances in the x and y directions, known as the spatial second-order moments, and computed according to the following equations:

$$\langle x^2 \rangle = \sigma_x = \frac{1}{P} \int_{-\infty}^{+\infty} \int_{-\infty}^{+\infty} (x - x_x)^2 E(x, y) \, dx \, dy \tag{B.4}$$

and

$$\langle y^2 \rangle = \sigma_y = \frac{1}{P} \int_{-\infty}^{+\infty} \int_{-\infty}^{+\infty} (y - y_c)^2 E(x, y) \, dx \, dy \tag{B.5}$$

and

$$\langle xy \rangle = \sigma_{xy} = \frac{1}{P} \int_{-\infty}^{+\infty} \int_{-\infty}^{+\infty} (x - x_c)(y - y_c) E(x, y) \, dx \, dy \tag{B.6}$$

Depending on whether the x and y variances are equal or not, the beam is either classified as stigmatic or astigmatic, respectively. All integrations in the aforementioned equations are performed over a rectangular area (Figure B.2) which is centered to the beam centroid, sized three times the beam widths, and directed parallel to the principal axes, which are the orthogonal directions of minimum and maximum extent: any power density is characterized by both their size and orientation. The former gives an indication about the beam widths along the 'x' principal axis:

$$d_{\sigma x} = 2\sqrt{2} \sqrt{(\sigma_x^2 + \sigma_y^2) + \text{sign}(\sigma_x^2 - \sigma_y^2)\sqrt{(\sigma_x^2 + \sigma_y^2)^2 + 4\sigma_{xy}^2}} \tag{B.7}$$

and along the 'y' principal axis:

$$d_{\sigma y} = 2\sqrt{2} \sqrt{(\sigma_x^2 + \sigma_y^2) - \text{sign}(\sigma_x^2 - \sigma_y^2)\sqrt{(\sigma_x^2 + \sigma_y^2)^2 + 4\sigma_{xy}^2}} \tag{B.8}$$

The latter introduces the so-called azimuthal angle, which provides a measure of the rotation of the principal frame with respect to a reference frame whose x and y axes are horizontal and vertical, respectively.

$$\phi = \frac{1}{2} \arctan \frac{2\sigma_{xy}^2}{\sigma_x^2 - \sigma_y^2} \tag{B.9}$$

Both Eqs. B.7, B.8, B.9 hold when $\sigma_x \neq \sigma_y$ [1]. The parameters described so far are represented in Figure B.1.

_____

[1] When the condition $\sigma_x = \sigma_y$ is met, the equations describing the diameters are modified substituting the last term with $16|\sigma_{xy}^2|$, while the azimuthal angle becomes $\phi = \text{sign}(\sigma_{xy})\pi/4$.
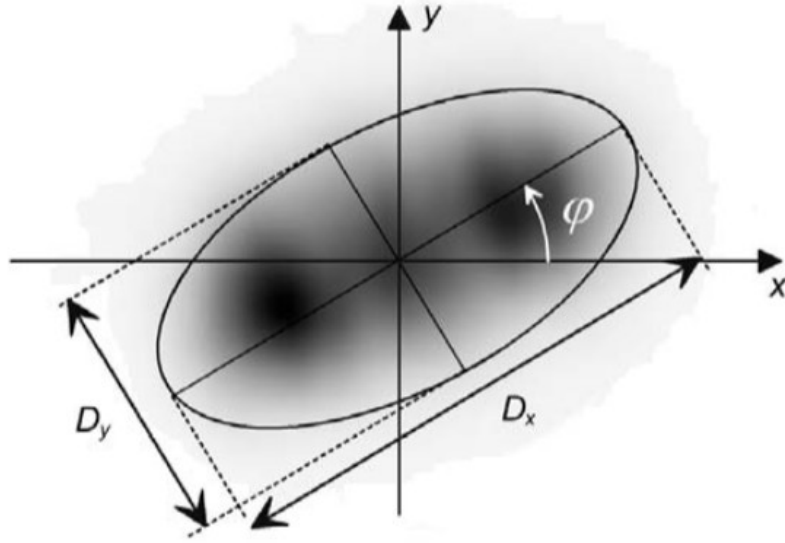
Figure B.1: Azimuthal angle and beam widths along principal axes.

Since the described procedure relates the size and position of the integration area to those of the measured power density distribution, which are initially unknown, an iterative approach is required, that has to be repeated until convergence of the result is obtained.
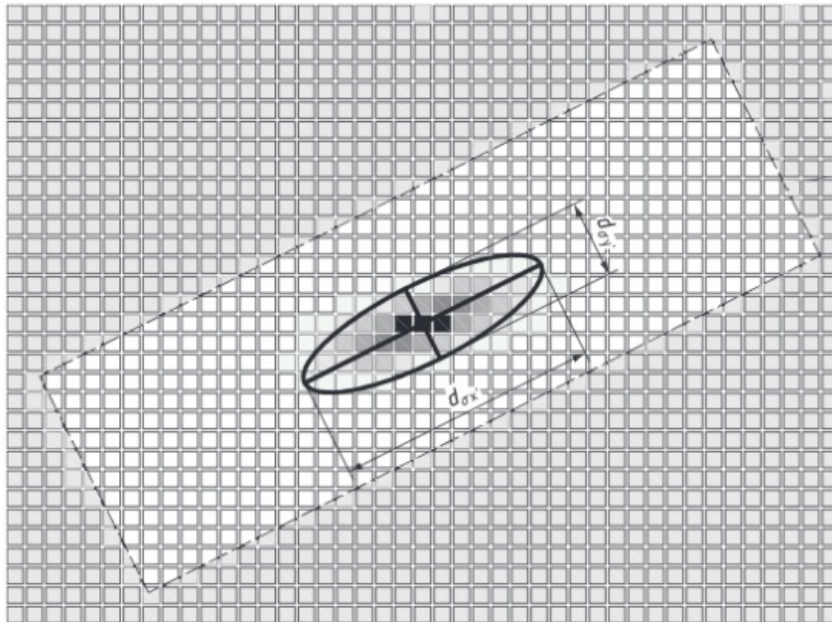

Figure B.2: Integration area

46

B.1.1 Background correction

An important aspect to be addressed is the management of background contributions, as these represent a source of noise in the measurement process. According to `ISO 11146-3`, the recorded signals can be divided into two parts: the true power density distribution $E(x, y)$ generated by the beam under test and a background map $E_B(x, y)$ generated by other sources:

$$E_{meas}(x, y) = E(x, y) + E_B(x, y) \tag{B.10}$$

where the background signal can be further divided into a homogeneous part, an inhomogeneous part, and a high-frequency component (which usually does not need correction). Among the various methods available for background determination, perhaps the simplest consists in its estimation using the pixel values located in the corners of the image. Having sampled them, the image can then be thresholded by labeling as unilluminated all pixels whose values are lower than the mean$+n_t\cdot$stdev.

B.2 Quality factor evaluation

The theoretical framework is that of multimode beams presented in Section 2.2. This time it is convenient to consider as the reference Gaussian the one having the same waist (known as illuminator) of the real beam. Having experimental values for the beam diameters d_σ at different axial locations z allows to express them as a function of position. The `ISO` standard then suggests fitting to the hyperboloid:

$$d_\sigma^2(z) = a + bz + cz^2 \tag{B.11}$$

which can be rewritten in terms of the beam waist diameter, the full divergence angle, and the location of the beam waist, yielding to:

$$d_\sigma^2(z) = d_0^2 + \Theta_\sigma^2(z - z_0)^2 \tag{B.12}$$

When Θ is expanded, the explicit dependence on M^2 is found to be:

$$d_\sigma^2(z) = d_0^2 + \left(\frac{4\lambda M^2}{\pi d_0}\right)^2 (z - z_0)^2 \tag{B.13}$$

In principle, M^2 measurements can be made using a CMOS imager to capture the changing beam profile at different points along the propagating direction at at least 10 different z positions, as stated by the `ISO 11146-1` document. Approximately half of the measurements shall be distributed within one Rayleigh length on either side of the waist, with the other half being distributed beyond two Rayleigh lengths from the waist.

B.2.1 Software validation

To validate the software routine developed to the computation of the M^2 factor, a dedicated simulation environment has been set up to reproduce the propagation of a known beam, specifically the one described in Section 3.1, which has been defined through the `GaussianBeam` class.

```python
# Include libraries
from raytracing import *
import laserbeamsize as lbs
import matplotlib.pyplot as plt
import numpy as np

# Define the laser source (nLight 1kW)
beam = GaussianBeam(q=complex(0, 0.389), n=1, wavelength
    =1068.7e-6, M2=2.9)
```

Listing B.1: Definition of the laser source

The validation has been performed by sampling the beam diameters at different axial positions along the propagation axis. This has been achieved by implementing a `for` loop iterated 20 times, where at each step the ABCD matrix describing the optical path has been updated by multiplying it by a `Space` element of width equal to 0.05 mm.

```python
    # Define the optical path
    path = LaserPath()

    # Define number of iterations and step size
    ietr = 20
    step = 1/iter

    # Initialize the variables
    M1   = Matrix(A=1, B=0, C=0, D=1)
    z    = [0]
    diam = [39.2]

    # Run the cycle
    for i in range(1, iter+1):
        M1 = Space(d=dz)*M1
        B  = M1.mul_beam(beam)

        z.append(dz*i)
        diam.append(2*B.w*1e3) # in microns
```

Listing B.2: Diameter sampling at various axial positions

The corresponding axial positions and computed beam diameters, stored in a Python list, have been subsequently converted into a `numpy` array, and provided as input to the `lbs.M2_radius_plot` function for the evaluation of the beam quality factor.

```
# M2 computation
lbs.M2_radius_plot(np.array(z)*1e-3, np.array(diam)*1e-6,
    1068.7e-9, strict=True)    plt.show()
```

Listing B.3: M2 evaliation

The resulting fit and calculated M^2 value, shown in Figure B.3, confirm the correct functioning of the computation routine.
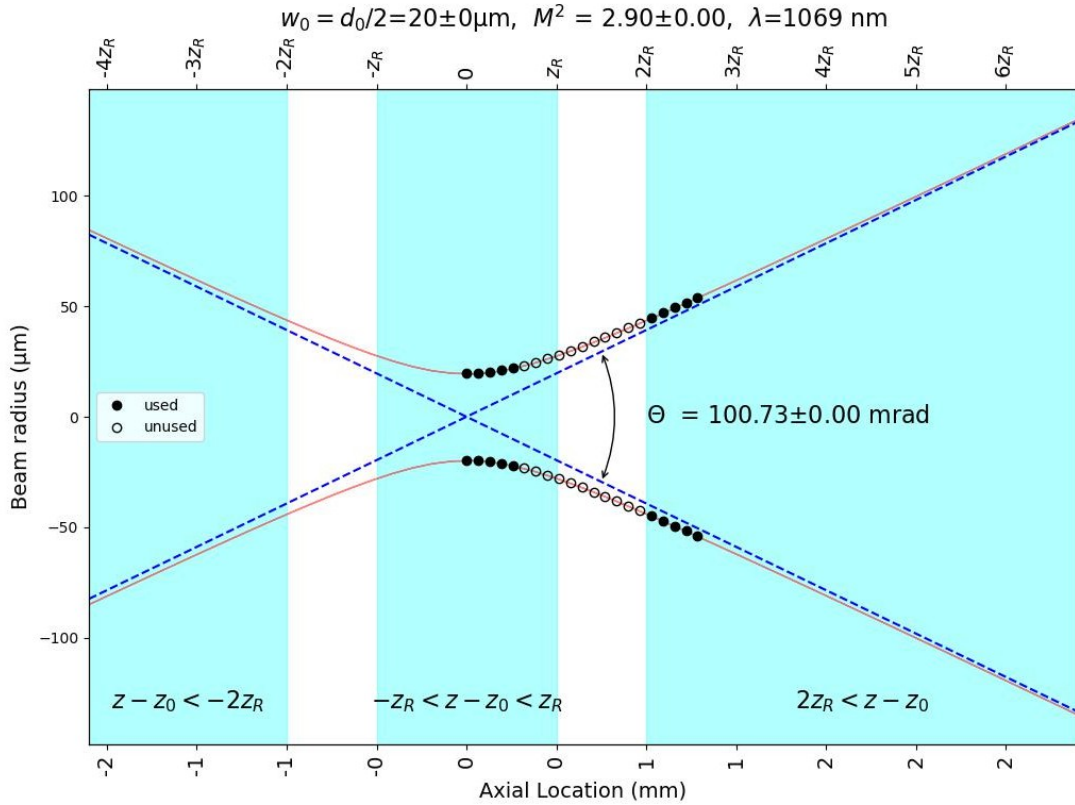

Figure B.3: M^2 validation from the nLIGHT® 1 kW module.

Bibliography

[1] A. Aversa, M. Moshiri, E. Librera, M. Hadi, G. Marchese, D. Manfredi, M. Lorusso, F. Calignano, S. Biamino, M. Lombardi, and M. Pavese, "Single scan track analyses on aluminium based powders," *Journal of materials processing technology*, vol. 255, pp. 17–25, 2018.

[2] M. Grasso, V. Laguzza, Q. Semeraro, and B. M. Colosimo, "In-process monitoring of selective laser melting: Spatial detection of defects via image data analysis," *Journal of manufacturing science and engineering*, vol. 139, no. 5, 2017.

[3] Newport Corporation, "Beam Focusing and Collimating," `https://www.newport.com/n/focusing-and-collimating`.

[4] V. Pineau Noël, S. Masoumi, E. Parham, G. Genest, L. Bégin, M.-A. Vigneault, and D. C. Côté, "Tools and tutorial on practical ray tracing for microscopy," *Neurophotonics (Print)*, vol. 8, no. 1, pp. 010 801–010 801, 2021.

[5] Interreg Europe, "Key Enabling Technologies (KETs) - A European Priority for Industrial Modernisation," `https://www.interregeurope.eu/find-policy-solutions/stories/key-enabling-technologies-kets-european-priority-for-industrial-modernisation`, 2021.

[6] P. Minetola, "Additive Manufacturing Systems and Materials," 2023, Lecture slides, Politecnico di Torino (Italy), slide 25.

[7] B. S. Institute, "BS EN ISO/ASTM 52900:2021: Additive manufacturing. General principles. Fundamentals and vocabulary," 2022.

[8] I. Gibson, D. Rosen, and B. Stucker, *Additive manufacturing technologies : 3D printing, rapid prototyping, and direct digital manufacturing*, 2nd ed. New York: Springer, 2015.

[9] T. T. Wohlers, I. Campbell, O. Diegel, R. Huff, J. Kowen, and W. A. (Firm), *Wohlers report 2022 : 3D printing and additive manufacturing global state of the industry*. Fort Collins, Colorado: Wohlers Associates, 2022.

[10] Metal AM, "Predicting the metal additive manufacturing market and breaking the hype cycle," https://www.metal-am.com/articles/predicting-the-metal-additive-manufacturing-market-and-breaking-the-hype-cycle/, 2023.

[11] H. Lee, C. H. J. Lim, M. J. Low, N. Tham, V. M. Murukeshan, and Y.-J. Kim, "Lasers in additive manufacturing: A review," *International journal of*

precision engineering and manufacturing-green technology, vol. 4, no. 3, pp. 307–322, 2017.

[12] A. Gaikwad, R. J. Williams, H. de Winton, B. D. Bevans, Z. Smoqi, P. Rao, and P. A. Hooper, "Multi phenomena melt pool sensor data fusion for enhanced process monitoring of laser powder bed fusion additive manufacturing multi phenomena melt pool sensor data fusion for enhanced process monitoring of laser powder bed fusion additive manufacturing," *Materials & design*, vol. 221, pp. 110 919–, 2022.

[13] M. Grasso and B. M. Colosimo, "Process defects and in situ monitoring methods in metal powder bed fusion: a review," *Measurement science & technology*, vol. 28, no. 4, pp. 44 005–, 2017.

[14] L. Chen, G. Bi, X. Yao, J. Su, C. Tan, W. Feng, M. Benakis, Y. Chew, and S. K. Moon, "In-situ process monitoring and adaptive quality enhancement in laser additive manufacturing: A critical review," *Journal of manufacturing systems*, vol. 74, pp. 527–574, 2024.

[15] X. Yang, Y. Li, and B. Li, "Formation mechanisms of lack of fusion and keyhole-induced pore defects in laser powder bed fusion process: A numerical study," *International journal of thermal sciences*, vol. 188, pp. 108 221–, 2023.

[16] M. Thiele, D. Dillkötter, J. Stoppok, M. Mönnigmann, and C. Esen, "Laser metal deposition controlling: melt pool temperature and target / actual height difference monitoring," *Procedia CIRP*, vol. 94, pp. 441–444, 2020.

[17] Y. Zhang, G. S. Hong, D. Ye, K. Zhu, and J. Y. Fuh, "Extraction and evaluation of melt pool, plume and spatter information for powder-bed fusion am process monitoring," *Materials & design*, vol. 156, pp. 458–469, 2018.

[18] B. Zhang, S. Liu, and Y. C. Shin, "In-process monitoring of porosity during laser additive manufacturing process," *Additive manufacturing*, vol. 28, pp. 497–505, 2019.

[19] J. Li, L. Cao, J. Xu, S. Wang, and Q. Zhou, "In situ porosity intelligent classification of selective laser melting based on coaxial monitoring and image processing," *Measurement : journal of the International Measurement Confederation*, vol. 187, pp. 110 232–, 2022.

[20] B. Cao, P. Hoang, S. Ahn, J.-o. Kim, H. Kang, and J. Noh, "In-situ real-time focus detection during laser processing using double-hole masks and advanced image sensor software," no. 7. Switzerland: MDPI AG, 2017, pp. 1540–.

[21] N. Harrop, H. Schwede, and K. G. Haensel, "Laser beam shape monitoring as a quality control tool in material processing," in *Lasers in Manufacturing Conference (LiM)*, 2017.

[22] S. Prahl, "laserbeamsize: a python module for ISO 11146 analysis of laser beams," Jun. 2025. [Online]. Available: https://zenodo.org/badge/latestdoi/107437651